THE OPTICAL PROPERTIES, ELECTRONIC STRUCTURE, AND PHOTOCONDUCTIVITY OF ARSENIC CHALCOGENIDE LAYER CRYSTALS

R. Zallen and D. F. Blossey

in *Optical and Electrical Properties of Compounds with Layered Structures*, edited by P. A. Lee. (Reidel publishers, Dordrecht, 1976), pp. 231-272.

THE OPTICAL PROPERTIES, ELECTRONIC STRUCTURE, AND PHOTOCONDUCTIVITY OF ARSENIC CHALCOGENIDE LAYER CRYSTALS

RICHARD ZALLEN and DANIEL F. BLOSSEY
Xerox Webster Research Center, Webster, N.Y., U.S.A.

1. Introduction

Among the many semiconducting layer crystals, As_2S_3 and As_2Se_3 are distinguished from several points of view. The two-dimensionally-extended network which forms the molecular building block in these crystals is held together by nearly purely-covalent bonding of the lowest connectivity (threefold coordination) compatible with a layer structure. Unlike graphite (with its π-bonding admixture), the bonding is entirely σ-type; unlike the transition-metal dichalcogenides (with their complicating d electrons), only *s* and *p* valence electrons are involved; and unlike the gallium chalcogenides (with their Ga—Ga bonds), only a single bond type occurs. Thus from a chemical-bonding and bonding-topology viewpoint, the arsenic chalcogenides are perhaps the simplest of layer crystals. From a crystallographic viewpoint, however, they are more complex than the other cases mentioned; their layer and crystal symmetries are low, and their unit cells contain relatively many atoms. (The number of atoms per *layer* unit cell in As_2S_3 is 10, compared to 2 for graphite, 3 for MoS_2, and 4 for GaSe.) This *combination* of

P. A. Lee (ed.), Optical and Electrical Properties, 231–272.

structural complexity and chemical simplicity in the arsenic chalcogenides provides a rare opportunity for the observation and elucidation of interlayer-interaction effects, and has been exploited in recent lattice-vibrational studies of the layer–layer coupling in these crystals [1, 2].

There is a different aspect of the interest in these two crystals which is somewhat apart from their layer-structure nature. This is their role as the crystalline analogs of the important chalcogenide glasses of the same chemical composition and short-range order. Amorphous As_2S_3 and As_2Se_3 are bulk glasses of considerable technological significance as infrared-transmitting window materials and as visible-sensitive large-area photoconductors. Because of this, their physical properties have, until recently, been much better characterized than those of the corresponding crystals. This abnormal situation in the relative level of information about and understanding of the crystalline and amorphous phases of these solids has provided much of the impetus for the recent work on the crystals, and this work has, in turn, contributed increased insight into the electronic structure of *both* forms. Access to this valuable tool of crystalline-amorphous comparison provides an extra dimension to the study of the arsenic chalcogenides which is unavailable for other layer crystals.

This chapter covers aspects of the electronic structure of As_2S_3 and As_2Se_3, and of the interaction of light with electronic excitations in these layer semiconductors. Our current understanding of these solids is reviewed and synthesized and, in addition to treating developments of recent years, we also include new material not available elsewhere.

The lattice structure of these crystals is introduced and analyzed in Section 2. Care is taken to differentiate between the crystal symmetry and the layer symmetry which coexist here as they do in all layer crystals, and which in this system (because of the low symmetries involved) lead to quite different and easily-distinguishable optical selection rules. It is the diperiodic (layer) symmetry which dominates the experimentally-observed optical properties. The electronic interband spectra, as determined by optical reflectivity and absorption measurements, by electron-beam energy-loss experiments, and by X-ray and UV photoemission studies, are discussed in Section 3. After a treatment of the fundamental absorption regime spanning the full ultraviolet region in which valence-electron excitation take place, the narrow region in the visible corresponding to excitations near the electronic threshold is examined in some detail.

The implications of the observed spectra for the underlying electronic structure are dealt with in Section 4. This discussion separates into three aspects: the band structure, interlayer effects, and the chemical bonding. Band-structure information of a very detailed nature is still lacking for these crystals, but statements can be made about the dominance of direct transitions at energies close to the bandgap, as well as about the existence of an approximate rigid-band relationship connecting As_2S_3 and As_2Se_3. Interlayer effects manifest themselves in the observed pressure dependence of the energy gap, as well as in the possibility of

Davydov splittings of intralayer levels. The chemical-bond approach to the electronic structure of these crystals derives strength from the availability of crystalline-amorphous spectral comparisons. Interpretations of the ultraviolet spectra in terms of bonding and nonbonding valence-band states, as well as questions concerning the degree of s-p hybridization in these states, are developed and scrutinized in this section.

While the optical spectra are dominated by the internal electronic structure of the individual layer, with interlayer effects appearing only in higher order, this is by no means the case for the electronic transport properties. In Section 5 we review the phenomena of dc and transient photoconductivity, as well as that of internal photoemission (photoinjection from metals) for transport perpendicular to the layers in crystalline As_2S_3. Carrier mobilities in this direction are inherently limited by the weakness of the layer–layer electronic interaction and are observed to be about 1 cm^2/volt-sec, a value typical of molecular crystals. A unique interference effect has been uncovered in the long-wavelength dc photoresponse observed with liquid electrodes, permitting the identification of photocurrents of surface origin. Field-dependent photogeneration is discussed and compared to current models. Finally, internal photoemission experiments are analyzed to yield the energies of the transport bands in the As_2S_3 crystal relative to the Fermi level in the evaporated metal contact. These data are found to contradict a current and popular ionicity picture for metal-insulator electrical interfacial behavior.

A brief summary of this chapter, including a discussion of gaps in our understanding and proposed fruitful directions for future research, is given in Section 6.

2. Structure and Symmetry

2.1. The orpiment structure

In his classic 1932 treatise setting forth what has since become known as the 'continuous-random-network model' for the structure of glasses, Zachariasen [3] presented a now-famous figure using a hypothetical A_2B_3 compound to provide a two-dimensional analogy for his ideas on the relationship between crystalline and amorphous solids. The A atoms were regarded as bonded to three nearest-neighbor B atoms, the B atoms to two nearest-neighbor A atoms, and his picture of the structure of the crystalline form is shown on the right side of Figure 1. Such a situation finds its realization in crystals formed from atoms of columns 5 and 6 of the periodic table, as might be expected from the simple 8-n rule for σ-type covalent bonding (n is the number of s and p valence electrons, 8-n the anticipated covalent coordination). The intralayer bonding in As_2S_3 and As_2Se_3 is highly covalent (electronegativity differences of 0.5 and 0.4, respectively, with only about 5% ionic character on the Pauling scale), and the 3, 2 coordination follows. Thus the bonding topology is accurately portrayed in Figure 1, although the actual structure is noncoplanar and much less symmetric than shown here.

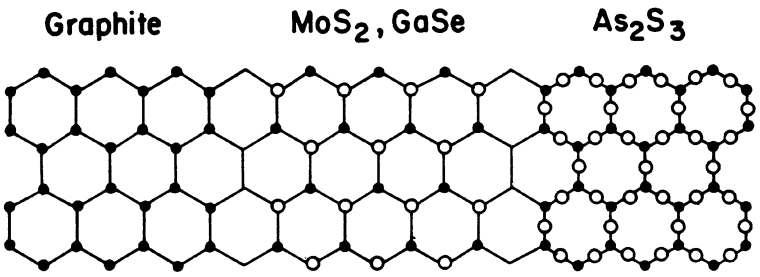

Fig. 1. Schematic bonding topology of the two-dimensionally-extended covalent networks which make up several classes of layer crystals. (After [2].)

To provide perspective, in Figure 1 we compare the bonding structure of the two-dimensionally-extended network (hereafter, 2_D-network) of the orpiment lattice to 2_D-network structures occurring in other types of layer crystals discussed in these volumes. All are schematically superimposed on the grid of a honeycomb lattice to emphasize the important role which the dominance of threefold coordination plays in the construction of a covalent network extended in two dimensions. Only in graphite are the atomic positions coplanar, and only the top half of the layer is shown for GaSe and MoS_2. In the GaSe structure a Ga—Ga bond connects the two halves of the layer, while the MoS_2 structure can be viewed as the result of coalescing bonded pairs of Ga atoms into single Mo atoms. These two types of 2_D-network crystals have more ionic character in their intralayer bonding than do the arsenic chalcogenides, and the cations are in higher-coordination setting (4 for Ga, 6 for Mo). In the graphite layers, of course, the bonding is even stronger than in diamond because of the contribution of the π electrons to the intralayer covalent bond. The As_2S_3 structure probably best epitomizes a covalent 2_D network composed solely of σ bonds of a single type.

The actual crystal structure of As_2S_3 [1, 4] (that of As_2Se_3 is closely isomorphic [5]) is shown in Figure 2, with the upper part providing a broadside view of a single layer and the lower part providing an edgewise view of two adjacent layers. The latter demonstrates the 'thickness' of the 2_D network. This internal structure of the layer is a consequence of the conformational requirements of the covalent bonding between nearest neighbors. Bond angles are intermediate between the values appropriate for sp^3 bonding (109°) and p^3 bonding (90°), averaging about 100° with a total range of about 15°. The 20-atom unit cell is shown outlined in the figure. It is intersected by two extended-layer molecules, a situation henceforth abbreviated by the phrase 'two layers per unit cell'.

The stacking of layers in the orpiment structure is determined by the geometry associated with providing the closest possible packing: the 'thick' portions of one layer tend to fit over the 'thin' portions of the next. This is the usual situation in layer crystals, but there is an interesting consequence here of the low symmetry of the individual layer in As_2S_3. In MoS_2-type and GaSe-type layer compounds, the

layer is a sandwich with the metal atoms in the interior and the chalcogen atoms forming the layer 'surfaces'. The S or Se atoms comprising each surface are arrayed in a triangular lattice so that (as is familiar, for example, from the different ways to arrange spheres in close packing) there are two sets of triangle-center positions available for the closest approach of the atoms forming the surface of the adjacent layer. This leads to many possible stacking sequences, all equivalently layer–layer close-packed, and these types of crystals do, in fact,

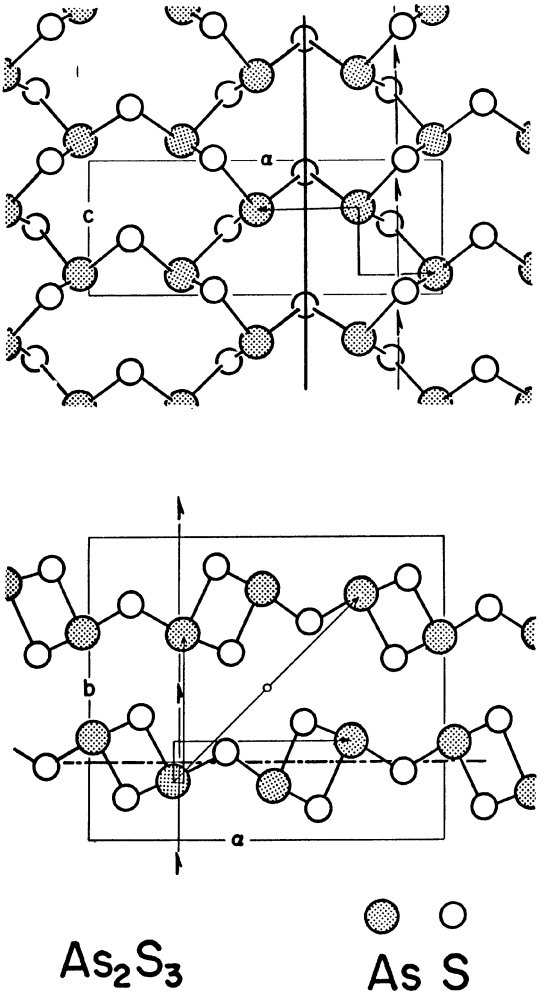

Fig. 2. The orpiment structure. The lower picture shows an edge-on view of the layers, the upper picture shows a broadside view of a single layer. Factor-group operations of the layer symmetry are indicated on the upper diagram, those of the crystal symmetry are indicated on the lower diagram. (After [1].)

exhibit very extensive polytypism. (PbI_2, a compound with a layer structure closely related to that of MoS_2, has revealed – thus far – some three dozen polymorphic variations corresponding to different stacking sequences [6]). In the arsenic chalcogenides, however, the low-symmetry structure of the isolated layer does *not* permit a multiplicity of equivalent layer–layer configurations, so that the stacking arrangement for optimum packing is unique. Polytypism is absent for As_2S_3 and As_2Se_3; no stacking arrangement different from the one shown in Figure 2 is observed.

The nature of the weak intermolecular forces which act between the layers and which hold such 2_D-network crystals together is poorly understood, although the assumption of van der Waals forces is widely made in the absence of better information. Raman-infrared studies of phonons in As_2S_3 and As_2Se_3 reveal an interlayer/intralayer force-constant ratio of about 0.06 [2, 7]. By contrast graphite, the most molecular (i.e. layer-like) in character of all layer crystals, is characterized by a corresponding force-constant ratio of 0.01.

2.2. Symmetry and diperiodicity

Symmetry analysis is a prerequisite to a discussion of optical selection rules in a crystalline solid. However it is important to recognize that in a *molecular* crystal *two* distinct symmetries coexist: the crystal symmetry, and the symmetry of the molecular unit in isolation. Layer crystals are, in fact, molecular crystals in which the molecular unit is *macroscopically* extended in two dimensions. For the most familiar class of molecular crystals, the molecular unit is *not* macroscopically extended but is finite on an atomic scale (S_8, N_2, C_6H_6, etc.) so that the molecular symmetry is a point group and its role in determining symmetry types and selection rules is well known. In a 2_D-network (layer) crystal, the molecular unit itself possesses *translational periodicity* in two dimensions, and the appropriate molecular symmetry is not a point group but is instead a *diperiodic* space group. The dominant role played by the diperiodic symmetry in layer crystals has only recently been appreciated [1, 2, 8]. The 80 diperiodic space groups apply to systems which possess two-dimensional translational periodicity but which are intrinsically three-dimensional in nature (the 17 purely 2_D space groups are a subset). Figure 3 shows the relationship of the diperiodic groups to other types of space groups.

The diperiodic group corresponding to the symmetry of a single layer in the As_2S_3 structure is, in Wood's listing [9], DG32. The space-group symbol is $Pnm2_1$, and the analogous triperiodic-group Schoenflies symbol is C_{2v}^7 [1]. The factor group of this orthorhombic layer symmetry consists of just four operations. Two are indicated in the upper part of Figure 2: a twofold screw axis parallel to *c*, and a mirror plane perpendicular to *a*. The others are the identity and a glide plane (indicated in the lower part of Figure 2) parallel to the layer. Note the presence of the screw axis and the glide plane, operations which reflect the

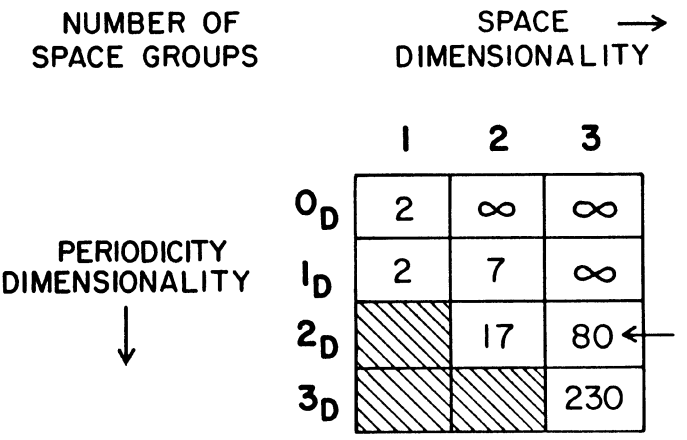

Fig. 3. The 80 diperiodic space groups set in relation to other types of space and point groups. The numbers in the table give the number of groups applying to m-dimensional objects ($m = 1, 2, 3$) possessing n-dimensional ($n = 0, 1, 2, 3$) translational periodicity. (After [2].)

three-dimensional character of the layer and which are forbidden to the 17 purely-2_D space groups.

The triperiodic crystal symmetry of the orpiment structure is $P2_1/n$ (C_{2h}^5). The factor group of the monoclinic crystal symmetry is illustrated on the lower part of Figure 2. It contains the identity and the glide plane in common with the layer-symmetry factor group, along with an inversion center located midway between layers and a twofold screw axis parallel to b (and perpendicular to the layers). The latter two crystal-symmetry operations interchange adjacent layers, and were of course absent from the layer symmetry. On the other hand, neither of the layer-symmetry operations illustrated on the upper part of Figure 2 is a symmetry operation of the crystal, since each is spoiled by the relationship between adjacent layers in the solid. It must be understood that neither the crystal nor the layer factor group is a subgroup of the other; they are instead simply *distinct* symmetries. Since adjacent layers are translationally inequivalent, the unit cell of the crystal structure contains 20 atoms instead of 10 as in the layer.

The dominance of the layer symmetry in determining the lattice-vibrational optical properties of As_2S_3 and As_2Se_3 has been clearly demonstrated by Raman-scattering and infrared-absorption experiments, as has the appearance of doublet spectral features associated with the fact that the crystal unit cell contains the unit cells of two adjacent layers [1, 2].

For the optical properties associated with electronic transitions, the visible and ultraviolet spectra of primary concern to us in this review, a demonstration of the dominance of the layer symmetry in these crystals is provided by the observed polarization dependences. Both the orthorhombic layer symmetry and the monoclinic crystal symmetry imply an optically biaxial material, that is, a material with three principal optical polarizations. This means that at each wavelength there are

three independent sets of optical constants corresponding to three orthogonal orientations of the electric field vector of the incident light. However, in a monoclinic system only one of the three principal axes of the dielectric-response tensor is fixed by symmetry, while in an orthorhombic system all three axes are symmetry-determined. In the crystal symmetry of As_2S_3 the only unique axis is the layer-stacking b-axis; the other two principal polarization directions are permitted to lie anywhere in the a-c layer plane and could, in fact, vary with varying photon frequency (dispersion of the optic axes). The a and c axes are nonspecial directions as far as the crystal symmetry is concerned, and thus would be expected to have no particular significance with respect to the optical properties. In fact, however, the visible and near-infrared experiments of Evans and Young [10] reveal that the two principal polarization directions in the layer plane are pinned precisely to the a and c axes. EY's data for the refractive indices are shown in Figure 4, along with some of ours which are in very good agreement

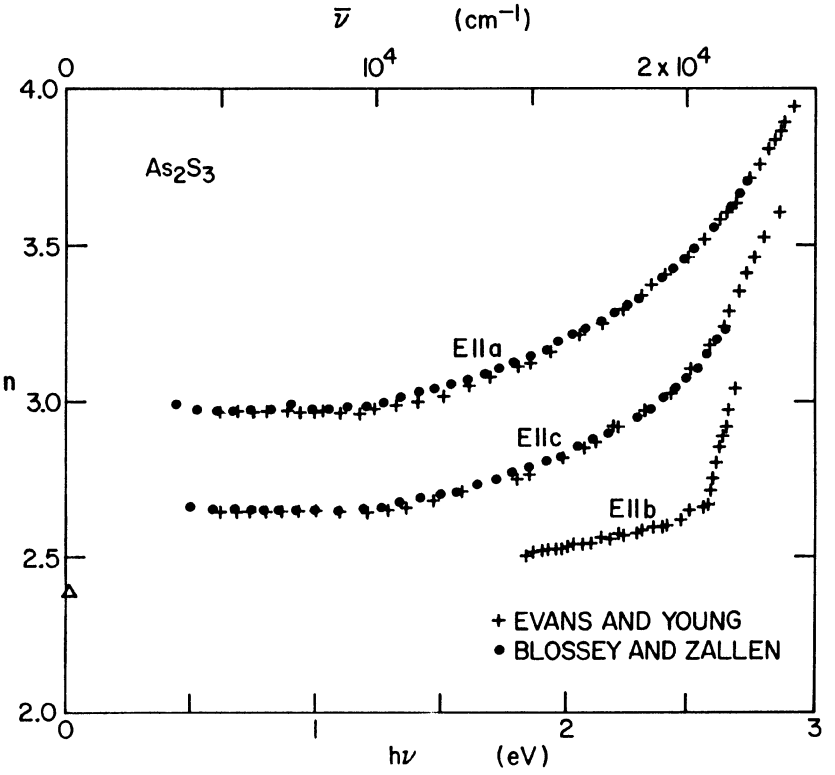

Fig. 4. Refractive indices in the transparent regime of As_2S_3 for the principal optical polarizations. The crosses shown for all three polarizations are from the work of Evans and Young [10], the solid dots are our own room-temperature results for the two in-plane polarizations, and the open triangle near the zero-frequency axis is from a capacitance measurement for the plane normal polarization [14].

where the two sets overlap. The indices for the in-plane polarizations are based on interference-fringe measurements and are more accurately known than the normal-to-plane index, obtained by EY using a convergent-light optic-figure technique. In the transparent regime shown here, the dispersion and polarization dependence of the refractive indices are controlled by the electronic transitions occurring in the fundamental absorption regime at higher energies.

In the context of the discussion of this section, the main message of Figure 4 is that the considerable optical anisotropy in the layer plane (refractive index for $E \| a$ some 12% greater than for $E \| c$, a very large birefringence) adheres to principal polarizations parallel to a and to c. This polarization behavior, which is rather odd from the viewpoint of the crystal symmetry, occurs as a natural consequence of the layer symmetry. The two operations of the diperiodic factor group which make the a and c axes special directions in the layer symmetry have been shown at the top of Figure 2. This dominance of the layer symmetry in the visible part of the spectrum (like that found in the far infrared) means that the symmetry types characterizing electronic eigenstates and the optical selection rules for electronic interband transitions (like those for phonons) are determined, to first order, by the properties of an isolated uncoupled layer. Optical effects of the weak interactions between layers show up in higher order.

3. Interband Spectra

3.1. Optical properties overview

In the wake of considerable experimental activity on these crystals in recent years, a great deal is now known about the optical properties of As_2S_3 and As_2Se_3. To place in perspective the visible and ultraviolet spectral regions of concern here, we display in Figure 5 a broad overview of the electromagnetic response function of As_2S_3. For convenience the optical 'constant' which we have chosen for representing the overall behavior is the normal-incidence reflectivity $R = [(n-1)^2+k^2][(n+1)^2+k^2]^{-1}$ (where $n-ik$ is the complex refractive index), shown for the in-plane polarization $E \| c$. The photon-energy or frequency scale is logarithmic and covers four decades corresponding to wavelengths ranging from a few hundred microns down to a few hundred angstroms. This curve has been constructed from reflectivity data measured in the far-infrared [1] and ultraviolet [11], from refractive-index data measured in the visible [10], and from electron energy-loss data measured in the voltage equivalent of the far ultraviolet [12]. Comprehensive spectral information over such a wide range is available for relatively few solids.

A dispersion plot such as that of Figure 5 should be read from right to left since it is cumulative with *decreasing* frequency. At very high frequencies the reflectivity is vanishingly small and the solid optically resembles free space since little in it

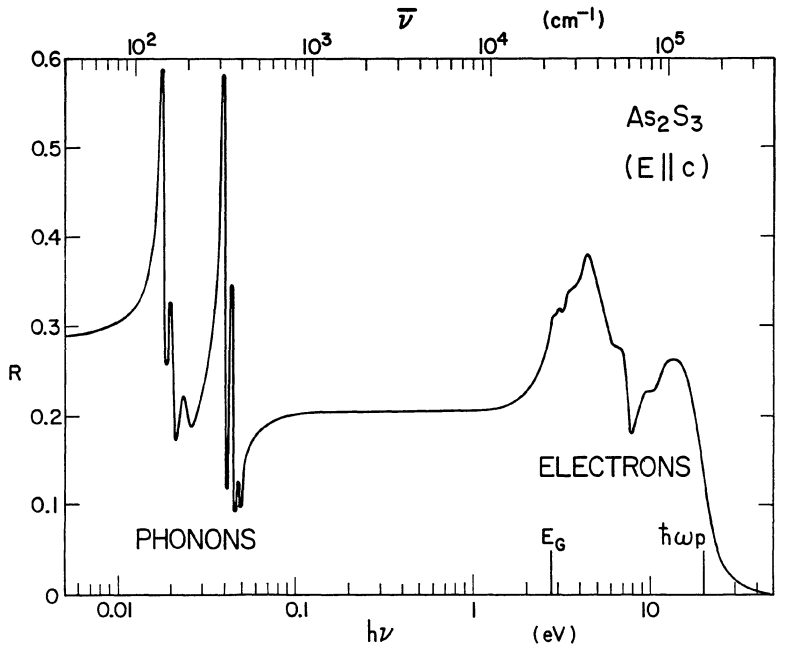

Fig. 5. Survey spectrum showing an overview of the optical properties of crystalline As_2S_3 from the far infrared to the far ultraviolet. The reflectivity for the in-plane polarization $E \| c$ has been composed, over a four-decade range of photon energies, from sources described in the text.

is capable of responding to such rapid electromagnetic oscillations. Way off to the right of Figure 5 there occur nuclear excitations in the gamma-ray region, and closer in there occur core-electron excitations in the X-ray region; both make negligible contributions to R on the reflectivity scale shown. Starting at about 20 eV the valence-electron excitations begin to drive up the reflectivity, then below the electronic threshold R levels off and there is a hiatus throughout the near-infrared transparent regime until the frequency becomes low enough for the advent of the atomic vibrations in the far infrared. At very low frequencies R approaches the asymptotic value $R_0 = [\varepsilon_0^{1/2} - 1]^2[\varepsilon_0^{1/2} + 1]^{-2}$, where ε_0 is the static dielectric constant and contains the integrated contributions of the various absorption processes.

Although the valence electrons provide the dominant contribution to the low-frequency reflectivity and dielectric constant, Figure 5 reveals a substantial contribution from the infrared-active phonons. Now while vibrational infrared activity reveals, of course, an electric dipole oscillating in synchrony with the atomic motion, for these solids this phenomenon must *not* be misconstrued in terms of ionicity. As noted earlier, the bonding within the 2_D-network molecules which make up the layer chalcogenides is almost entirely covalent. The infrared effective charges implied by the non-negligible oscillator strengths of the one-phonon optical absorption processes observed in these crystals is *dynamic* charge

[13] associated with displacement-induced charge redistribution, and is *not* connected with any appreciable static "ionic" charge residing on the atoms as a result of equilibrium charge transfer.

Table 1 lists the current best estimates of the static dielectric constants of As_2S_3 and As_2Se_3, along with the approximate breakdown into electronic and vibrational contributions. Information about the out-of-plane polarization $E \| b$ is sketchy relative to that available for the in-plane polarizations, but values are listed for As_2S_3 based on capacitance measurements of ε_0 [14] and a recent infrared-reflectivity estimate for $\Delta\varepsilon$(vibrational) [15]. The deduced value of $\varepsilon_\infty^{1/2}$ is plotted on Figure 4 as n_b ($h\nu = 0$), and is reasonably consistent with the refractive-index data of Evans and Young.

3.2. The fundamental absorption regime

The fundamental region of optical absorption associated with electronic transitions in a semiconducting solid extends roughly from the valence-band → conduction-band energy gap E_G to the plasma energy $\hbar\omega_p$ corresponding to the density of valence electrons. Reflectivity data over most of this region is presented in Figure 6 for the in-plane polarizations $E \| c$ and $E \| a$, as obtained in near-normal-incidence experiments by Zallen *et al.* on cleaved natural As_2S_3 crystals and on as-grown vapor-deposited As_2Se_3 crystals [11]. Also included in Figure 6 are reflectivity spectra of the amorphous forms of these solids, since a comparison of these spectra to those of the crystals will yield insight into the electronic structure of the latter.

Absorption spectra derived by Kramers-Kronig analyses of these data [16] are shown in Figure 7. First the gross features should be noted. The primary electronic threshold, which brings to an end the infrared transparent regime, occurs at about 3 eV for As_2S_3, 2 eV for As_2Se_3. (The small and spurious negative absorption at lower photon energy provides a measure of the experimental and

TABLE I

Comparison of the electronic and vibrational contributions to the static dielectric constants of crystalline As_2S_3

		In-plane polarizations		Out-of-plane polarization
ε	$h\nu$	$E \| a$	$E \| c$	$E \| b$
ε(vacuum)	$>10^2$ eV	1.0	1.0	1.0
$+\Delta\varepsilon$(electronic)	2–20 eV	7.8	6.0	4.7
$=\varepsilon_\infty$	~0.5 eV	8.8[a]	7.0[a]	5.7
$+\Delta\varepsilon$(vibrational)	0.01–0.05 eV	3.3[b,c]	3.7[b,c]	0.2[c]
$=\varepsilon_0$	$<10^{-3}$ eV	12.1	10.7	5.9[d]

[a] Ref. [10].
[b] Ref. [1].
[c] Ref. [15].
[d] Ref. [14].

KK-transform truncation errors of this procedure.) Interband transitions produce the strongest interactions of these solids with light, driving the optical absorption coefficient α up to a level of order $10^6\,\mathrm{cm}^{-1}$. About 5 eV above the primary threshold, a second absorption threshold is seen in both crystals and also in both corresponding glasses. This basic feature is discussed in Section 4.3 in terms of the intralayer chemical bonding. Between the two thresholds in the crystals, but absent in the glasses, are sharp features which are band-structure effects associated with van Hove density-of-states singularities caused by critical points in the Brillouin zone. These features, emphasized in Figure 6 and further discussed in Section 4.1, demonstrate that direct (wavevector-conserving) transitions dominate the optical properties of these layer crystals as they do for the covalently-bonded 3_D-network semiconductors of groups IV, III–V, and II–VI.

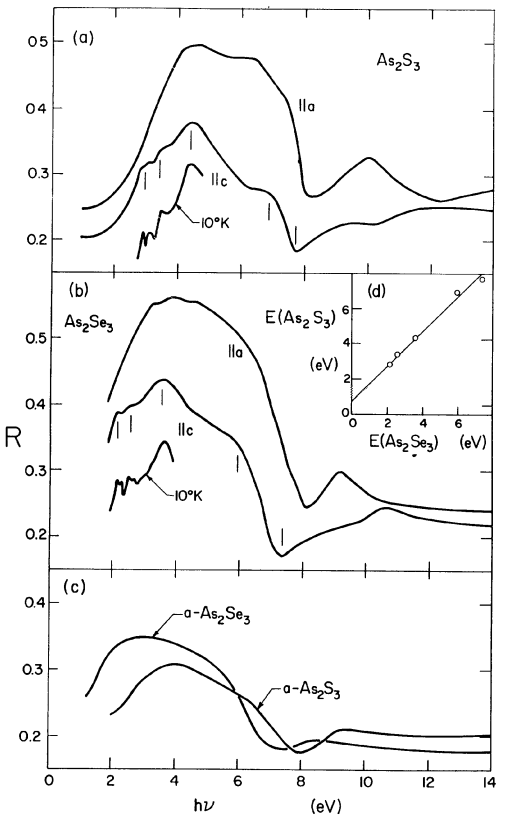

Fig. 6. (a), (b) Interband reflectivity spectra of crystalline As_2S_3 and As_2Se_3. The 10 K spectra shown for $E \| c$ are downshifted in reflectivity by 0.10, for clarity. (c) Reflectivity spectra of the amorphous forms. (d) Plot of interband energies of crystalline As_2S_3 versus energies of crystalline As_2Se_3. (After [11].)

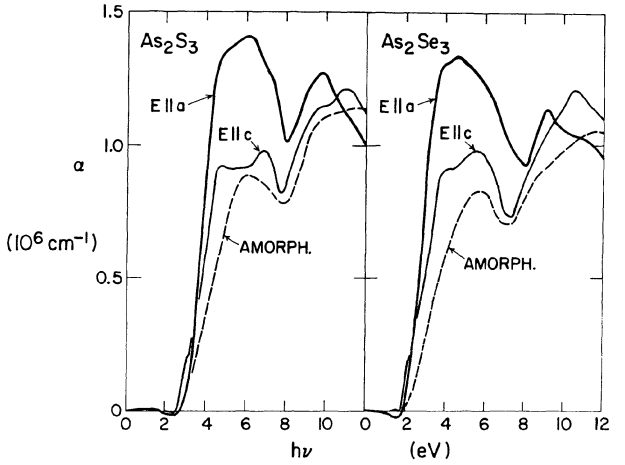

Fig. 7. Absorption spectra of crystalline As_2S_3 and As_2Se_3 for the in-plane polarizations, as well as of the amorphous forms, derived by Kramers-Kronig transformation of the data of Figure 6. (After [16].)

The spectral range covered by the optical data of Figures 6 and 7 does not exhaust the contribution of the valence electrons. Measurements to higher energies have recently been obtained by a nonoptical technique. Perrin *et al.* [12] have carried out electron energy-loss experiments on thin tape-cleaved As_2S_3 crystals using a 40 keV electron beam. Their results for the energy-loss function are shown in Figure 8. This function is closely related to the negative imaginary part of the reciprocal of the complex dielectric function, $-\mathrm{Im}\{\varepsilon^{-1}\}$, and the other response functions can be derived by Kramers-Kronig analysis in a way entirely analogous to that used for optical reflectivity data. While much less accurate and of lower resolution than optical data (for example, the van Hove fine structure cannot be seen and even the second main threshold at 7–8 eV is unclear), these results do extend our information to 35 eV and also provide some data about $E \| b$. Electron energy loss, like optical absorption, involves an electric dipole matrix element (although longitudinal rather than transverse as in the case of light).

Another important probe in this energy regime is the use of X-ray photoemission spectroscopy (XPS, sometimes also referred to as ESCA), in which the kinetic energy of photoemitted electrons is analyzed to yield information about the valenceband density of states. XPS experiments on crystalline As_2S_3 and As_2Se_3 have been carried out by Fisher [17], and on crystalline and amorphous As_2S_3 by Bishop and Shevchik [18]. Figure 9 shows Fisher's data on the crystals, obtained with incident photons of 1254 eV. Photoemission is shown plotted against electron kinetic energy, with the zero set at the high-energy cutoff (top of the valence band). Bishop and Shevchik's data on crystalline and amorphous As_2S_3 is shown in Figure 10. These latter spectra have been approximately corrected for

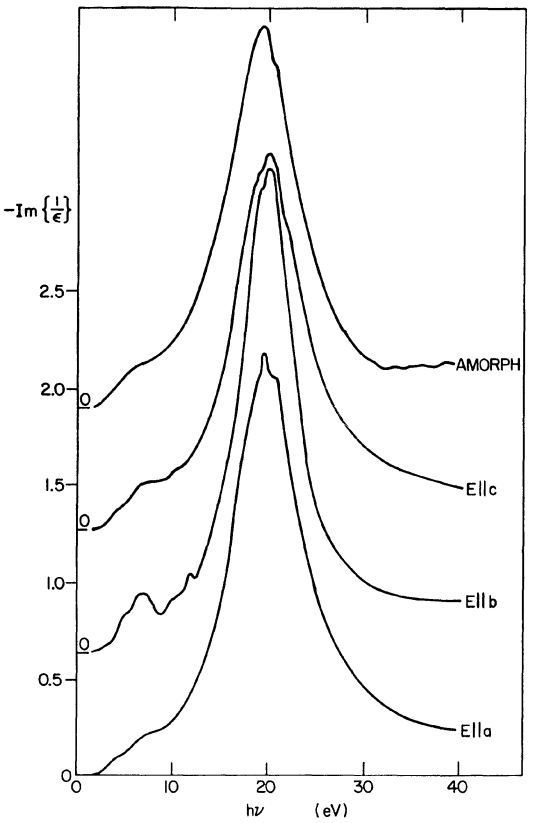

Fig. 8. Energy-loss function of As_2S_3 for $E \| a$, b, c, and also of the amorphous form, observed by Perrin *et al.* [12] using a 40 keV electron beam.

inelastically-scattered secondary electrons by subtracting off a linear background, which accounts for the apparent difference in shape between the corresponding As_2S_3 curves of Figures 9 and 10 (which in actuality agree well).

These spectra will come in for further discussion and interpretation in Section 4. Now it suffices to note only the broad features. Included among these are the two main absorption thresholds exhibited by each of the curves of Figure 7, the two or three main bands exhibited by the densities-of-states of Figures 9 and 10, and the overall striking crystal-amorphous similarities of Figures 6, 7, and 10. All of these have clear implications with respect to the electronic structure.

3.3. The edge-absorption region

In this section we focus down on the narrow spectral region in the vicinity of the threshold for interband transitions. Edge-absorption spectra are of special interest in semiconductors because of the variety of fine-structure effects exhibited and

because of what they reveal about the electronic states at the frontiers of the forbidden zone. Photoconductivity is a phenomenon to be discussed in depth in Section 5 of this chapter, and here the action of interest takes place at photon energies near E_G.

Edge-absorption spectra of crystalline As_2S_3 and As_2Se_3 [11], at 300 K and at 10 K, and for $E \| c$ and $E \| a$, are shown in Figure 11. In contrast to Figure 7, the energy scale is now in tenths of eV rather than in eV, and the absorption scale is now logarithmic and extends down to levels four or five orders of magnitude lower than that characteristic of the fundamental absorption region. On this closeup view, the modest smearing-out exhibited by the spectra of the corresponding amorphous solids (shown at room temperature in Figure 11, decreasing temperature has little effect on the glasses) appears quite pronounced. Since on this level of detail the amorphous spectra differ significantly from the crystalline, these will not be discussed further here.

Steep but rather featureless at room temperature, the absorption edges of these crystals develop clearcut structure at low temperature. For As_2Se_3 at 10 K, a pronounced knee appears strongly at 2.19 eV ($\alpha \sim 2 \times 10^4\ cm^{-1}$) and, further down on the edge, a weaker but equally-clear knee is seen at 2.01 eV ($\alpha \sim 5 \times 10^2\ cm^{-1}$). For As_2S_3 at 10 K, the $E \| c$ edge-absorption displays a strong knee at 2.90 eV ($\alpha \sim 4 \times 10^4\ cm^{-1}$), and there is also an indication of a weaker washed-out knee at about 2.78 eV. The anatomical term 'knee' is being used here to denote a

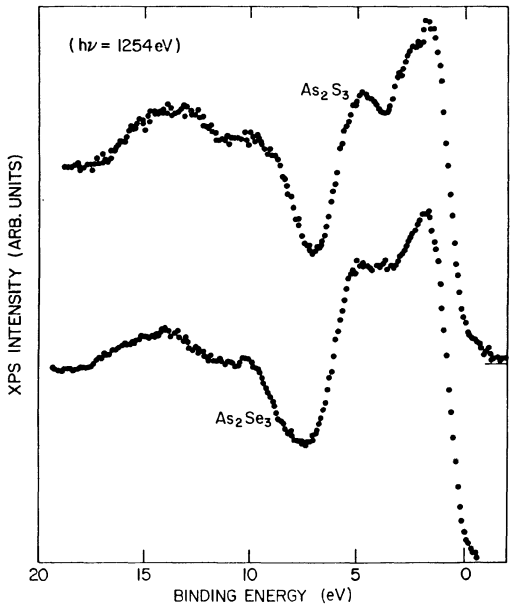

Fig. 9. X-ray photoemission spectra obtained by Fisher [17] for the valence bands of crystalline As_2S_3 and As_2Se_3.

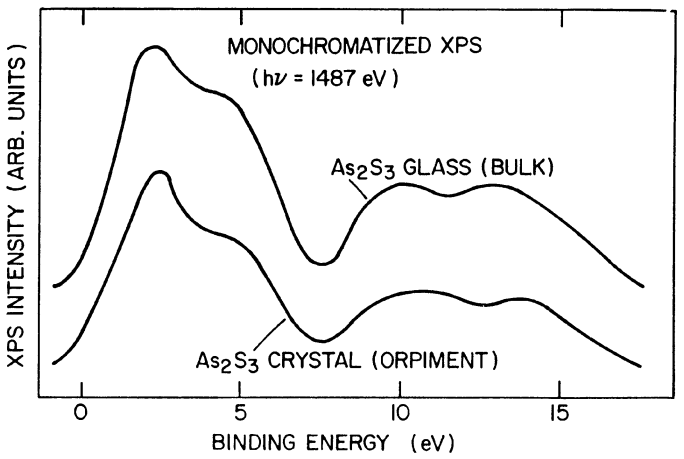

Fig. 10. XPS data obtained by Bishop and Shevchik [18] to compare the valenceband densities of states of crystalline and amorphous As_2S_3.

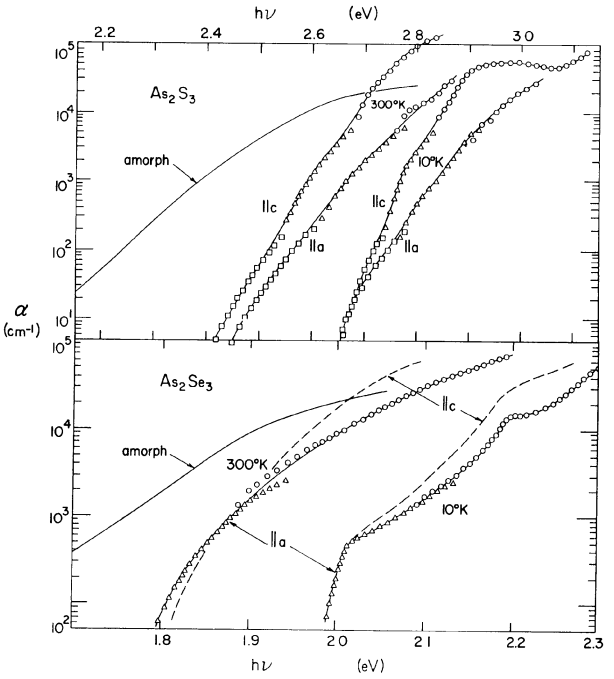

Fig. 11. Edge-absorption spectra of As_2S_3 and As_2Se_3 crystals at 300 K and at 10 K, as well as of the glasses at room temperature. (After [11].)

specific type of spectral feature in the absorption edge, namely a sudden *decrease* in slope of $\alpha(h\nu)$.

Dichroism within the layer plane is very evident in the edge region for As_2S_3 with $\alpha(E\|c)$ exceeding $\alpha(E\|a)$ by an order of magnitude near 2.9 eV at low temperature (and near 2.75 eV at room temperature). It should be noted that although the onset of interband absorption processes occurs first for $E\|c$, Figure 7 reveals that $\alpha(E\|a)$ overtakes $\alpha(E\|c)$ at photon energies just off to the right of those shown in Figure 11 and then proceeds to dominate throughout most of the fundamental absorption region in the ultraviolet. This is the reason that the refractive index n in the transparent region is larger for this polarization (Figure 4), since $n-1$ at long wavelengths λ is proportional to $\int \alpha(\lambda)\, d\lambda$.

The high absorption features of Figure 11 ('high absorption' here means $\alpha > 10^4$ cm^{-1} or, in more fundamental terms, $\varepsilon_2 \equiv \text{Im}\{\varepsilon\} > 1$) are strong enough to show up in the reflectivity spectrum. Figure 12 shows the evolution of the $E\|c$ reflectivity of As_2S_3 upon cooling to 10 K [19]. The first piece of spectral structure, which develops into a very well-defined 2.9 eV peak at low temperature, corresponds to the high-absorption knee in $\alpha(\hbar\nu)$. No structure is seen at this energy in the low-temperature reflectivity for $E\|a$, again consistent with Figure 11. Thus the polarization selection rules for this 2.9 eV interband transition in As_2S_3 appear to be $E\|c$-allowed, $E\|a$-forbidden. Low-temperature reflectivity spectra for As_2Se_3 indicate a similar conclusion for the corresponding transition at 2.2 eV, although the absorption-edge distinction between the two in-plane polarizations is less marked for this crystal. The 2.0 eV edge in As_2Se_3, like the 2.8 eV edge in As_2S_3, is too weak ($\varepsilon_2 \sim 0.01 \ll 1$) to be discernible in reflectivity.

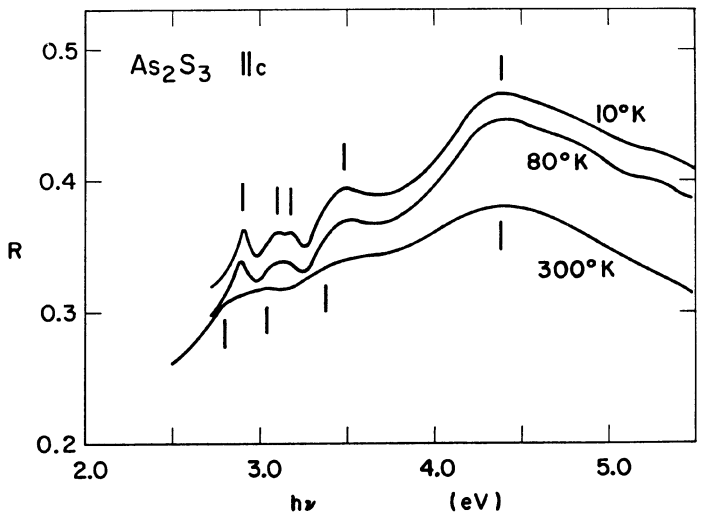

Fig. 12. Evolution, with decreasing temperature, in the sharpness of critical-point direct-transition features in the interband reflectivity of As_2S_3 [19].

4. Electronic Structure

4.1. The band structure

It must be frankly admitted that we know very little about the *detailed* electronic energy-band structure of crystalline As_2S_3 and As_2Se_3. Although chemically quite simple (only two types of atoms present), the structural complexity of these crystals (which leads to the interesting aspects discussed earlier in Section 2) makes life very difficult for the band theorist concerned with electron wave functions and energy-versus-momentum dispersion relations. If, as a first cut, one wants to calculate the two-dimensional band structure $E(\mathbf{k})$ specifying the variation of electronic energy eigenvalue E as a function of in-plane wave-vector $\mathbf{k}$ for a single layer (i.e., in the limit of vanishing interlayer interaction), then it is necessary to contend with at least 28 bands to account for the 56 valence electrons in the 10-atom layer unit cell! *Twice* as many (atoms, electrons, bands) must be dealt with in an attack on the three-dimensional band structure. This situation appears to have put off the theorists, despite the interest in and importance of these crystals and the availability of optical data with which to test any calculations. In spite of this there are several interesting things which can be said about the band structures directly on the basis of the experimental spectra alone, and we shall now proceed to do this.

The first point is illustrated in the insert (d) shown on Figure 6. The close similarity between the two pairs of polarization-dependent interband spectra shown for the crystals on this figure and on Figure 7 clearly suggests an intimate connection between the electronic structures of these two solids. In the insert we have plotted the photon energies of prominent features in the sulfide spectrum against the photon energies of the corresponding features in the selenide spectrum. Despite the naiveté of this idea, we find that the results are well described by a straight line of slope unity. The implication of this is the existence of an approximate rigid-band relationship between the electronic structures of the two crystals. In other words, we conclude that whatever their detailed character, the energy band structure of crystalline As_2S_3 can be roughly derived from that of As_2Se_3 by rigidly separating valence and conduction band by an additional 0.7 eV [the vertical-axis intercept in Figure 6(d)].

A question of substantial interest about the band structure of a semiconductor is whether the energy gap between the valenceband maximum and the conductionband minimum corresponds to a direct ($\mathbf{k}$-conserving) or indirect ($\mathbf{k}$-nonconserving) transition, i.e., the question of whether or not the two band extrema occur at the same point in the zone. For example, a consideration of some technological interest is that a direct-gap semiconductor is a candidate for a laser material while an indirect-gap semiconductor is not. Conversely, an indirect-gap semiconductor permits the occurrence of electron-hole 'droplets' (i.e., the coalescence of photoexcited electron-hole pairs into a condensed phase) while a direct-gap material does not. For the layer chalcogenides, some controversy has

existed on this point. Several early optical workers [10, 20, 21] suggested that these crystals possessed indirect gaps, usually on the basis of obtaining several apparently 'linear' regions in a plot of $\alpha^{1/2}$ versus $h\nu$ (corresponding to the expected functional form for phonon-assisted indirect transitions). The difficulty with those interpretations was the fact that the purported indirected thresholds occurred at absorption levels orders of magnitude too large. In actuality, all of the optical structure thus far observed in crystalline As_2S_3 and As_2Se_3 must be attributed to direct transitions.

Absorption-edge features associated with direct and indirect transitions are very well documented, and the characteristics of *shape* and *strength* of the $\alpha(h\nu)$ structure produced by the two processes are enormously different and readily distinguished. A threshold produced by a direct gap occurs as a steep edge ending in a sharp knee (often with an excitonic peak at low temperature) at an absorption level of order 10^3–10^5 cm^{-1}. In marked contrast, an indirect threshold occurs as a *foot* (sudden *increase* in slope) instead of a knee (slope decrease) in $\alpha(h\nu)$, and takes place at very low absorption of order 0.1–10 cm^{-1}. It is therefore inescapable to conclude that the low-temperature thresholds seen in Figure 11 at 2.0 and 2.2 eV for As_2Se_3 and at 2.9 eV for As_2S_3 are due to *direct* transitions.

It would be useful to extend the results of Figure 11 down to lower α's in order to put to rest the question of possible lower-energy indirect transitions. However it is noteworthy that the sharpness of the absorption edges of these crystals at the lowest α's of Figure 11 are typical of the steep absorption tails produced by phonon-assisted direct transitions *below* a direct threshold, rather than the much more gradual increase in α typically observed *above* an indirect threshold. Thus the present best information indicates that crystalline As_2S_3 and As_2Se_3 are both direct-gap semiconductors. Assuming, then, that the lower-energy direct threshold seen in each crystal defines the bandgap, we have $E_G(T \approx 0)$ equal to 2.01 eV for As_2Se_3 and 2.78 eV for As_2S_3. Estimating the room-temperature bandgaps by an isoabsorption approximation yields an E_G of about 1.85 eV for As_2Se_3 and 2.6 eV for As_2S_3.

4.2. Interlayer effects

We continue with a discussion of an aspect which is special to these semiconductors as layer crystals. Grant and Yoffe [22], and Kolomiets and Raspopova [23], have found that the optical bandgap of As_2Se_3 *decreases* rapidly under pressure. This behavior runs counter to that which is familiar from our experience with the 3_D-network germanium-family semiconductors of groups IV, III–V, and II–VI, in which the bandgap normally *increases* with pressure: $dE_G/dP > 0$ [24]. We believe that a negative pressure coefficient ($dE_G/dP < 0$) for the bandgap of a layer semiconductor will prove to be the rule for such 2_D-network solids. For example, Besson *et al.* [25] have recently reported this to be the case for GaSe.

The essential part of our argument for the generality of a compression-induced decrease of E_G in a semiconducting layer crystal is outlined in Figure 13. Let us

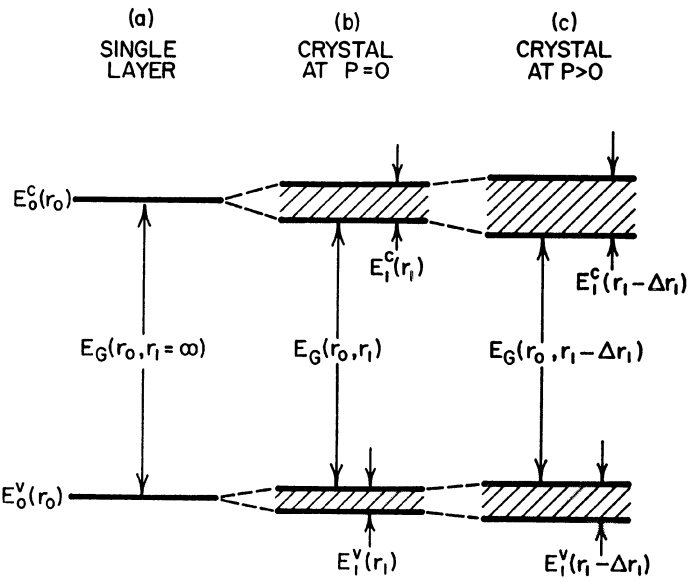

Fig. 13. Illustration of the connection between layer–layer interactions and the negative pressure coefficient of the bandgap in a layer crystal.

suppose that a single, i.e. totally-isolated, extended layer possesses a two-dimensional band structure in which $E_0^c(r_0)$, $E_0^v(r_0)$, and $E_G(r_0) = E_0^c(r_0) - E_0^v(r_0)$ are the energies corresponding to the conductionband minimum, the valenceband maximum, and the bandgap, respectively. Here r_0 represents the covalent bond length, the most important parameter of the layer's internal structure. For As_2Se_3, r_0 would be the As—Se bond length, and $E_0^c(r_0)$ and $E_0^v(r_0)$ would be the band extrema in the $k_a - k_c$ plane. Now we turn on the interlayer interaction, using the familiar type of gedanken experiment, by bringing together a large assembly of layers from an initially-infinite layer–layer separation to a final separation corresponding to the actual layer stacking in the crystal. The interlayer spacing is denoted by r_1, and the new bandgap is denoted in Figure 13(b) by $E_G(r_0, r_1)$. The bandgap of the isolated layer is denoted in Figure 13(a) by $E_G(r_0, r_1 = \infty)$. Throughout this discussion an intralayer quantity is indicated by subscript 0, an interlayer quantity by subscript 1.

In the crystal, each electronic level of the isolated layer spreads out into a narrow band of levels as the Brillouin zone develops a third dimension normal to the original two-dimensional zone. The bandwidths along this new k-direction (k_b for As_2S_3 and As_2Se_3), for the two single-layer states which bounded the original bandgap, have been labelled $E_1^c(r_1)$ and $E_1^v(r_1)$ in Figure 13(b). These bandwidths depend only on r_1, vanish for $r_1 = \infty$, and increase with decreasing r_1.

Figure 13(c) indicates what happens with applied hydrostatic pressure. Pressure decreases the very soft interlayer spacing ($r_1 \rightarrow r_1 - \Delta r_1$) but has negligible effect

on the stiff bond-length r_0. Lattice-vibrational and pressure-Raman studies of layer crystals [1, 7, 26] revealed that $\Delta r_0/r_0$ is one to two orders of magnitude smaller than $\Delta r_1/r_1$. Thus the bandgap under pressure may be regarded, to lowest order, as $E_G(r_0, r_1 - \Delta r_1)$, and is reduced from the value of the zero-pressure bandgap $E_G(r_0, r_1)$ because of the increased interlayer-overlap bandwidths $E_1^c(r_1 - \Delta r_1)$ and $E_1^v(r_1 - \Delta r_1)$. Hence the negative dE_G/dp.

To make contact with the normal situation for a germanium-family semiconductor, we note that in a 3_D-network solid r_0 is alone as the key structural parameter, that r_0 now decreases appreciably with pressure (no softer springs are present to absorb the brunt of the compression), and that a decrease in r_0 means an increase in the bonding-antibonding average gap between the valence and conduction bands. Since the average gap increases significantly with pressure, the minimum gap E_G usually follows suit in exhibiting a positive pressure coefficient [24].

Figure 13(b) can also be used to illustrate another type of interlayer-interaction band-structure effect proposed by Lisitsa *et al.* [27] in analogy with vibrational Davydov splittings observed for As_2S_3 and As_2Se_3 by Zallen *et al.* [1]. Because these crystals have two layers per unit cell, each intralayer vibrational frequency gives rise to a pair of closely-spaced frequencies in the crystal. The electronic analog is Figure 13(b) with each pair of levels corresponding, not the extremes of a band of energies for states dispersed along an axis in k-space (as in the previous discussion), but to a discrete pair of energies at the *same* k-vector. Such doublets should give rise to multiplets or fine-structure energy shifts in the direct-transition interband spectra.

4.3. The chemical bonding

Although we have seen that only a limited amount is known about the energy bands in these crystals, this does not exhaust our knowledge of their electronic structure. Another approach to the nature of electronic states in solids, one which can yield a different (and perhaps deeper) insight into the nature of the electronic states, is the chemical-bond approach [28]. It has been with this in mind that spectra of the amorphous forms have been included in Figures 6–10. As_2S_3 and As_2Se_3 glasses possess no long-range order but have the same short-range order [29] as the crystals (threefold coordination for As, twofold coordination for S or Se, as in Figures 1 and 2). Spectral features which *survive the loss of long range order*, such as the second major threshold at $E_G + 5$ eV, must reflect a basic and localized characteristic of the electron states on a chemical-bonding level.

We can, in fact, associate the two-threshold absorption spectra exhibited by all four of these solids (Figure 7) with the circumstance that the valence bands in these semiconductors are composed of nonbonding as well as of bonding states. This is different from the simpler situation obtaining in germanium-family semiconductors, and the chemical-bonding energy-level schematic for Ge is given in Figure 14(a) to provide a point of departure. The formation of the solid from

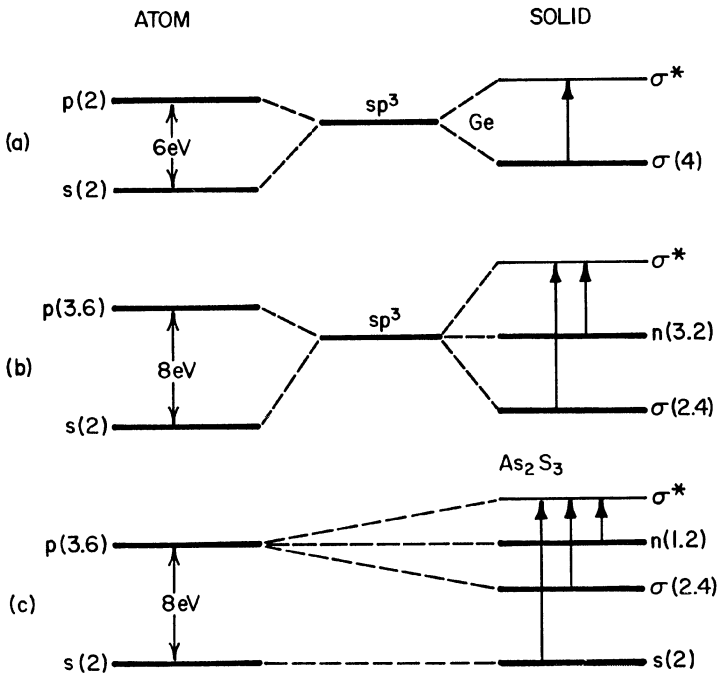

Fig. 14. Representations of simple models for the atomic origin of crystal orbitals in (a) Ge and (b), (c) As_2S_3. (b) Shows the hybridized-orbital view of the genealogy of bonding (σ) and nonbonding (n) electronic levels within the covalently-bonded layer in orpiment, while (c) shows the corresponding p-orbital-only view. Numbers in parentheses give the average number of electrons per atom for each occupied level. Overlap splitting, but not overlap broadening, is indicated for the solid; the discrete levels shown on the right side represent centers of gravity of energy bands.

the isolated atoms is visualized in two steps: (1) the 'preparation' of the s^2p^2-configuration atoms by the formation of four tetrahedrally-equivalent sp^3 hybrids, and (2) the bringing together of the atoms along the bond directions to split apart (and to broaden into bands, an aspect omitted from the figure for clarity) the bonding and antibonding levels. The simplified arithmetic of the bonding energetics is that (1) costs about 6 eV per atom (one $s \rightarrow p$ promotion) while (2) gains about 10 eV per atom, with a net gain of about 4 eV per atom (or 2 eV per bond) to account for the solid's cohesive energy. The gain in (2) results from the four valence electrons being lowered by half the overlap-induced bonding-antibonding splitting (average gap) of about 5 eV. In Ge, as well as in all of the tetrahedrally-coordinated A^nB^{8-n} semiconductors with 4 electrons per atom, all of the s and p valence electrons of the original atoms populate bonding states in the crystal. As discussed below, this is *not* the case in layer-type semiconductors since the covalent coordination within the extended layer is lower than four.

The analogous bonding picture for the arsenic chalcogenides is depicted in

Figure 14(b). Since the level diagram is for an average atom, fractional numbers now appear for the electrons per atom in some of the bands. The argument of hybridization followed by overlap bonding proceeds as before with the development of bonding and antibonding orbitals except that now, because of the low coordinations, there are also orbitals unaffected by atom–atom overlap. These nonbonding or 'lone pair' states lie intermediate in energy between the bonding and antibonding states. Three of the five outer-shell electrons of each arsenic atom may be regarded as contributed to the three bonds, with the other two occupying a lone pair orbital directed away from the bonds in the fourth, missing, tetrahedral direction. Similarly two of the six electrons of each chalcogen atom reside on the bonds, with the other four occupying two lone pair orbitals.

The arithmetic of the energy balance is only slightly more complicated than before. Hybridization to sp^3 directed orbitals now formally require three-quarters of an $s \rightarrow p$ promotion for each As and one-half of an $s \rightarrow p$ promotion for each S or Se. Since the $s \rightarrow p$ promotion energy is about 7 eV for As, 9 eV for S, and 10 eV for Se [30], the cost per atom of hybridization is about 5 eV. The energy gain per atom, provided by the 2.4 bonding electrons, is $1.2E(\sigma \rightarrow \sigma^*)$ where $E(\sigma \rightarrow \sigma^*)$ is the bonding—antibonding splitting. As indicated below, $E(\sigma \rightarrow \sigma^*)$ is at least as large as 7–8 eV so that the net gain is at least 4 eV per atom (or 3 eV per bond).

Figure 14(b) supplies the gist of the explanation [16] of the two principal interband thresholds, seen in As_2S_3 at 3 eV and 8 eV, and in As_2Se_3 at 2 eV and 7 eV. The first threshold corresponds to transitions from the *nonbonding* valence band to the antibonding conduction band, the second corresponds to transitions from the *bonding* valence band to the conduction band. Using a notation borrowed from molecular spectroscopy, these are $n \rightarrow \sigma^*$ and $\sigma \rightarrow \sigma^*$ transitions, respectively. In Ge-family semiconductors, only $\sigma \rightarrow \sigma^*$ transitions are present and no second threshold occurs in this region of the ultraviolet.

The essential aspect of this interpretation of the electronic structure is the separation, within the valence band, between higher-energy nonbonding states and lower-energy bonding states. This point now seems to be reasonably well established, although some questions about and variations of the simple picture do exist. For example, there has been some concern about the fact that bandgap photons can induce photocrystallization or photodecomposition in the chalcogenide glasses [31]. The idea here is that if bonds are broken then $\sigma \rightarrow \sigma^*$ transitions are involved, and this has motivated Chen [32] to point out that molecular-orbital studies can yield results indicative of appreciable bonding/nonbonding mixing. However there is every reason to believe that $n \rightarrow \sigma^*$ transitions should also be extremely effective in enhancing the crystallization rate of the metastable amorphous forms, since these transitions strongly destabilize the bonds whose antibonding orbital is excited, and since the amorphous $\rightarrow$ crystalline energy barrier is very small.

A modified version of the bonding/nonbonding model of the valence band,

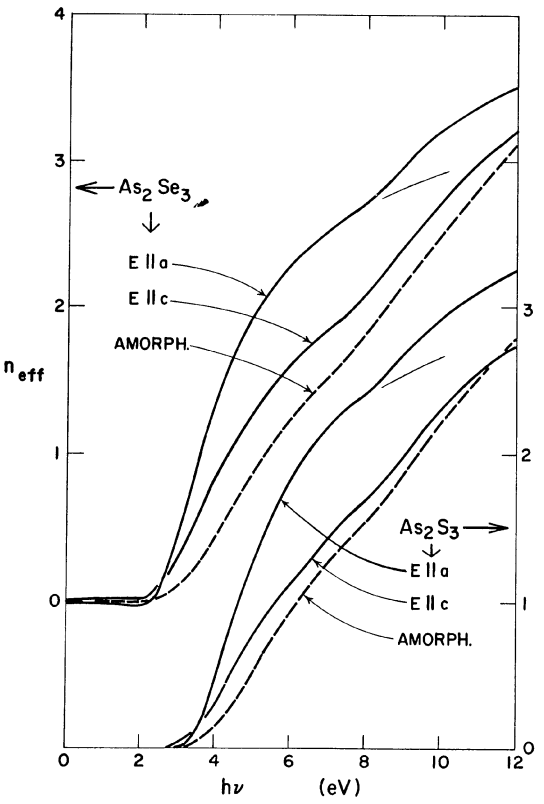

Fig. 15. Effective number of electrons per atom contributing to the optical absorption spectra of crystalline and amorphous As_2S_3 and As_2Se_3, derived by sum-rule integration of the data of Figures 6 and 7. (After [16].)

proposed recently on the basis of X-ray photoemission studies [18], is indicated in Figure 14(c). The suggestion here is that *s-p* hybridization is unimportant and that the bonding–antibonding splitting occurs entirely within the *p*-orbital manifold. The basis for this suggestion, in which the atomic *s* states are regarded essentially as core states, is the broad band seen in Figures 9 and 10 at bonding energies of 10–15 eV. This deep band is attributed to *s* states, and its absence in UV photoemission data [33] is ascribed to matrix-element effects.

Several difficulties exist with this picture. The $s \rightarrow p$ energy spacing in atomic As, S, and Se is 7–10 eV, scarcely larger than the 6 eV $s \rightarrow p$ spacing in Ge. The valence bands in As_2S_3 and As_2Se_3 are about 17 eV wide (accepting the X-ray photoemission data), compared to 12 eV for the valenceband width in Ge. It seems unreasonable to assert that, although they play an important bonding role

in Ge, the s electrons are somehow deep and out of play in the chalcogenides. Moreover, in addition to offending our chemical sensibilities, the viewpoint of Figure 14(c) is also contradicted quantitatively by the spectral analysis presented in Figure 15 [16]. This figure displays a quantity $n_{\text{eff}}(\omega)$ which is given by $(2/\pi)(1/\omega_p^2)\int_0^\omega \omega\varepsilon_2(\omega)\,\mathrm{d}\omega$, where ε_2 is the imaginary part of the dielectric constant and ω_p is the electronic plasma frequency corresponding to a concentration of one electron per atom. This monotonically-increasing function, which is referred to as the optically-derived effective number of electrons per atom, is based on the sum rule that requires $n_{\text{eff}}(\infty)$ to equal the total electronic density. The n_{eff} curves of Figure 15, shown for the in-plane polarizations for the crystals and for the amorphous forms as well, are from the work of Drews *et al.* [16] and correspond to the ultraviolet spectra of Figures 6 and 7.

It is seen that the $n \rightarrow \sigma^*$ contribution to $n_{\text{eff}}(\hbar\nu)$ has not yet reached saturation when the $\sigma \rightarrow \sigma^*$ transitions enter at 8 eV, but extrapolation of the $E \| a$ curves (lying highest at 8 eV and therefore closest to saturation for the first band) indicate the exhaustion of $n \rightarrow \sigma^*$ transitions at a value of about 3–3.5 electrons per atom. This result is consistent with the hybridized-orbital picture (Figure 14b) but not with the p-orbital-only picture (Figure 14c), since without the s electrons there are only 1.2 nonbonding electrons per atom instead of 3.2. Thus we must choose Figure 14(b) as the proper, if oversimplified, chemical-bond picture of the electronic structure.

5. Photoconductivity

5.1. Surface photoresponse

The previous sections, in addressing the optical properties and electronic structure of the arsenic chalcogenide layer crystals, have been interlaced with a persistent theme. This is the idea that it is the molecular (layer) structure and not the crystal structure which dominates the optical properties, i.e., that the electronic response of the crystal differs by only a minor perturbation from the response of a single layer. In this section we provide some counterpoint. In dealing with photoconductivity, we must concern ourselves with the fate of the excitation *after* the optical absorption process, and are addressing the question of what portion of the absorbed energy results in a photocurrent. Photoconductivity is a three-step process involving optical absorption, charge separation of electron-hole pairs (carrier generation), and transport of the carriers through the solid. Each sequential step in this process occurs over a larger time frame than the previous step, and is thus more apt to suffer from competition with alternative pathways for the excitation. Photoconductivity efficiency is related to the speed of the photoresponse since the photocurrent mechanism must compete with energy-loss and carrier-loss mechanisms. In the following, we will see that the speed of the photoresponse is directly related to the transport characteristics of the solid, which are, in turn, largely limited by the weak links. For transport perpendicular

to the layers, the case of interest to us here, this means that the weak layer–layer coupling is controlling. Thus the interlayer interactions dominate key aspects of the photoconductivity experiments to be discussed in this section, a situation opposite to that applicable to the optical properties treated earlier.

Some photoconductivity work has been done on crystalline As_2Se_3 [21, 23] but our discussion will be limited to As_2S_3 because this work is much more complete and the phenomena observed should be similar for both crystals. In the following we review studies of the photoconductivity of crystalline As_2S_3 in which are observed both electron photoinjection from surface states [34, 35] and field-dependent bulk generation of photocarriers [34]. The surface states occur at energies within the crystal's forbidden gap (and may be present as defect states in the bulk of the corresponding amorphous form). Field-dependent photogeneration has been observed in amorphous Se [36] and As_2S_3 [37] and other amorphous molecular solids [38], but is also present in molecular crystals such as anthracene [39]. This effect is clearly not a result of disorder but appears to be a more general property of low-mobility solids, as the frequency-dependent ac conductivity may well be [14].

Photocurrent spectra of As_2S_3 crystals were measured for both polarizations of incident light with respect to the layer plane ($\dot{E} \parallel c, E \parallel a$), and for both field polarities relative to the illuminated (010) surface. The samples were tape-cleaved to thicknesses of order 1–6 μ, and their thicknesses were calculated from the positions of the interference maxima in the transmission spectra (using the refractive index data shown previously in Figure 4). The calculated thicknesses are considered to be accurate to within 5%, as estimated by the differences between the thicknesses calculated separately from the $E \parallel c$ and $E \parallel a$ interference-fringe spectra.

A typical photoyield spectrum (photocurrent normalized to incident photon flux) for light polarized $E \parallel a$ and current flow normal to the layers ($J \parallel b$) is displayed in Figure 16, along with the transmission spectrum of the crystal. Because the crystals used in this study were cleaved to thicknesses only a few times greater than the optical wavelengths propagating in the solid, easily-resolvable light intensity modulations were superimposed on all spectra due to interference effects from multiple internal reflections from the crystal surfaces. These interference effects are pronounced because of the large refractive-index mismatches at crystal-air and crystal-liquid interfaces, and because of the optical quality of the cleaved surfaces. The photoyield spectra for both in-plane polarizations are shown in Figure 17, with the interference oscillations being intentionally suppressed so that the spectra do not depend on sample thickness. In these measurements, conducting aqueous salt solutions were used as contacts. The cell schematic is shown as an insert in Figure 18. Also included in the figure are the edge-absorption spectra of crystalline As_2S_3 for the two in-plane polarizations. The photocurrents follow the edge-absorption spectra near and above the absorption edge, but not at lower photon energies. The photoyield displays a long

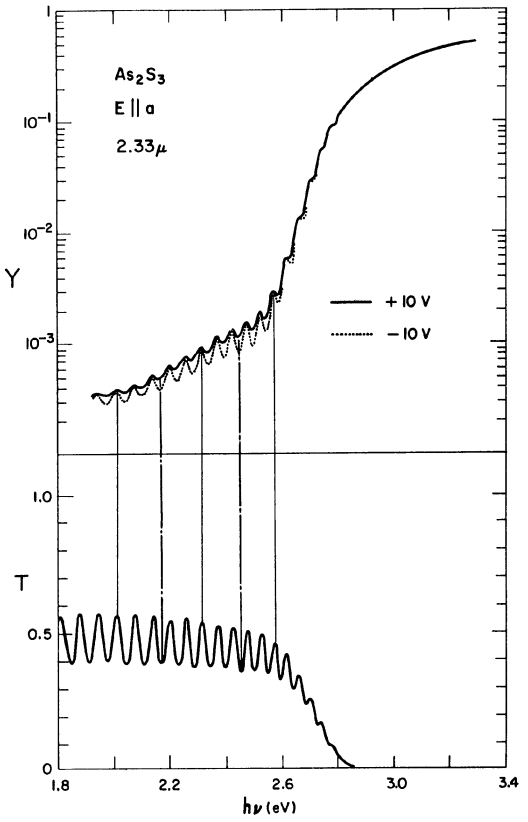

Fig. 16. Photoyield (Y) and transmission (T) spectra of a thin As_2S_3 crystal between liquid electrodes, with incident light polarized $E \| a$ and with photocurrent flowing $\| b$. The photoyield is the photocurrent density normalized to incident photon flux.

polarization-independent tail, extending well below the threshold for bulk absorption. We will show that this long wavelength photoresponse is due to electron injection from surface states.

In the crystal's transparent region, the photocurrents exhibit interference peaks in a one-to-one correspondence to those seen in transmission. This long-wavelength photoresponse decreases only gradually with decreasing photon energy, in pronounced contrast to the optical absorption of the bulk crystal which plummets steeply to negligible values in this region. The very existence of a photoresponse in the absence of bulk absorption, as well as the polarization independence of this long-wavelength response, in themselves suggest an injection process; but we will see that the interference effect provides us with even more specific and unmistakable evidence for this.

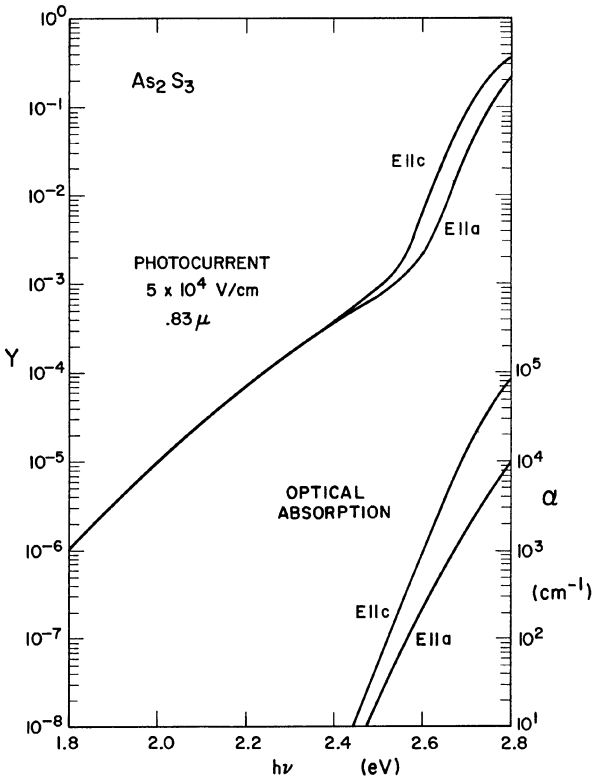

Fig. 17. Photoyield spectra (Y) of a thin As_2S_3 crystal for $E \| c$ and $E \| a$, with the interference fringes in the long-wavelength photoresponse tail averaged out. Shown for comparison are the corresponding edge-absorption spectra (α).

Examination of the less-than-bandgap photocurrents of Figure 16 reveals a definite bias dependence of the amplitude of the interference oscillations in the photocurrent spectra. When a negative voltage is applied to the illuminated surface, the interference minima are deeper than those observed when the bias is reversed (or when the cell is turned around). If the currents are produced in the bulk there should be no change upon bias reversal, so that the effect must be of surface origin. But why should a surface effect exhibit a difference upon bias reversal since the liquid electrode cell is symmetric and the crystalline surfaces are identical? (The crystal symmetry of As_2S_3 is centrosymmetric.) The answer lies in the fact that the optical excitation is effective in creating photocarriers at only *one* of the two surfaces, and the interference effect on the light intensity is *not the same* at the two surfaces. Let us now calculate the light intensity as a function of wavelength, for wavelengths at which bulk absorption is negligible, at both the front and back surfaces. This analysis will show that the light intensity is more

strongly modulated by the interference at the front surface than it is at the back surface, with deeper minima and the same maxima. In fact, the interference effect tells us that the *less-than-bandgap photocurrents always originate at the negatively biased surface.*

What follows is a calculation of the effects of the multiple reflections and transmissions occurring when a nonabsorbing material of thickness d and refractive index n intercepts, at normal incidence, a light beam propagating in a medium of refractive index n'. In our case, n is an in-plane refractive index for As_2S_3 as given in Figure 4 (2.97 for $E \| a$ and 2.65 for $E \| c$) and n' is the refractive index of the salt solution (constant at 1.34 in the visible). If the incident beam has an amplitude (electric vector) of unity and the primary reflected and transmitted beams at $x = 0$ have amplitudes r and t respectively, then the boundary conditions requiring continuity of transverse electric vector and power flow give

$$1 - r = t \quad \text{and} \quad n' = n'r^2 + nt^2, \quad n' \to n,$$

where we have defined the reflected beam's electric vector to be inverted with respect to the incident beam. Similarly, since the amplitude of the primary beam incident on the second surface, at $x = d$, has amplitude t, the amplitudes of the primary reflected and transmitted beams at $x = d$ are tr' and tt' respectively. Then the boundary conditions requiring continuity of the transverse electric vector and power flow give equations similar to those above, or

$$1 - r' = t' \quad \text{and} \quad n = nr'^2 + n't'^2, \quad n \to n'.$$

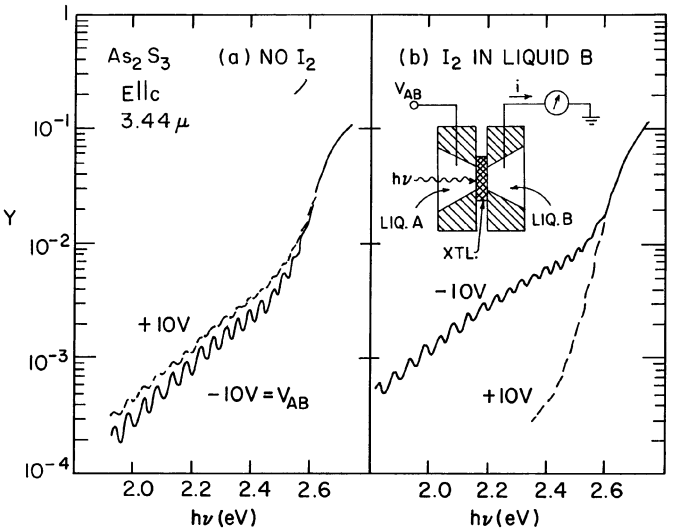

Fig. 18. Quenching of the long-wavelength photoresponse of an As_2S_3 crystal by the presence of iodine dissolved in the back electrode.

All subsequent reflections must satisfy the identical boundary conditions with the relative amplitudes being $(1, r, t)$ when the wave passes from $n' \rightarrow n$ and $(1, r', t')$ when the wave passes from $n \rightarrow n'$. Solving the above equations we find that

$$r = -r' = \left(\frac{n-n'}{n+n'}\right) \quad \text{and} \quad nt = n't' = \frac{2nn'}{n+n'}.$$

Calculating intensities at the two surfaces involves summing all the amplitudes including appropriate phase factors. Rays which have undergone multiple internal reflections will have a phase ϕ_m relative to other beams at the same surface given by $\phi_m = m\beta$, where m is an integer, β is $4\pi nd/\lambda$, and λ is the free-space wavelength of the light. For instance, the electric vector $E(0)$ at $x = 0^-$, is given by the sum of all the electric vectors at that point in space.

$$\begin{aligned} E(0) &= 1 - r - r'tt'e^{i\beta} - r'^3tt'e^{2i\beta} - r'^5tt'e^{3i\beta} - \cdots \\ &= (1-r)(1+re^{i\beta})/(1-r^2e^{i\beta}). \end{aligned}$$

Similarly at $x = d^+$,

$$\begin{aligned} E(d) &= tt' + r'^2tt'e^{i\beta} + r'^4tt'e^{2i\beta} + \cdots \\ &= (1-r)(1+r)/(1-r^2e^{i\beta}), \end{aligned}$$

whereby the light intensities are given by

$$I(0) = |E(0)|^2 = (1-r)^2(1+r^2+2r\cos\beta)/(1+r^4-2r^2\cos\beta),$$

$$I(d) = |E(d)|^2 = (1-r^2)^2/(1+r^4-2r^2\cos\beta).$$

Using the above equations, we are now in a position to understand the bias dependence of the long-wavelength photoresponse of crystalline As_2S_3. We have argued that the bias dependence (plus the negligible bulk absorption) in the photoresponse tails excludes bulk effects, leaving surface effects to provide the only possibilities for the underlying mechanism. Since the two surfaces are identical chemically, we have looked elsewhere and found that there is an asymmetry in the interference effect. Specifically, from the above equations it follows that the intensity maxima ($\cos\beta = 1$) at the front and back surfaces are of equal amplitude but that the intensity minima ($\cos\beta = -1$) are *deeper at the front surface* than at the back. Since the polarity dependences of Figure 16 show that the interference oscillations are strong when the front surface is negatively-biased and weak when the back surface is negatively-biased, it follows that the long-wavelength photocurrents originate at the negatively-biased surface. This means that the less-than-bandgap photoresponse corresponds to *electron photoinjection from surface states.*

A related experiment [35] provides striking confirmation of the above interpretation. It is known that atomic iodine can be produced by photodissociation of I_2 molecules in solution [40], and that such free iodine is a powerful electron scavenger. Figure 18 shows the results of a photoresponse experiment on As_2S_3 in

which iodine has been introduced into the back electrolyte. With the back surface biased negatively so that the electron injection is from the back surface, the presence of iodine causes a dramatic quenching of the electron injection photocurrent. This means that the iodine radicals, formed by photodissociation of I_2 in solution, effectively deplete the surface states of electrons. This is dramatic evidence for the surface origin of the long-wavelength photoresponse, and also confirms that it corresponds to photoinjection of electrons (rather than holes).

5.2. Bulk and transient photoresponse

Measuring steady state photocurrents is the most direct method of examining the carrier generation step. If a carrier is generated (escapes initial recombination), and is not trapped in surface or deep bulk traps, it will transit the solid and during this process will be measured as current. The major difficulty in the interpretation of steady state currents is the possibility of trapping which can occur either in the bulk or at the surface (contact). If a significant amount of charge is trapped, the internal field will be difficult to define. This effect is usually recognized by photocurrent decay from its initial value, when the light is first turned on, to a lower steady-state value. It is important that the current be observed during the first few transits to make an unambiguous interpretation. Secondly, if trapped charge accumulates at one of the contacts, secondary injection can ensue leading to photoinduced currents not directly related to the primary generation step. These currents should show the classic gain-current time response starting at a low value of current and increasing to a higher steady-state value. These high-gain photocurrents will not show linear light-intensity dependencies.

With liquid contacts there are no apparent complicating contact effects [14] and the surface photoresponse is linear with field, consistent with the field dependence of injection currents [41]. For strongly absorbed light, the photocurrent shows a zero-field intercept plus a linear field term consistent with the Onsager model [38, 39]. This is shown in Figure 19. The Onsager model predicts

$$Y = \exp\left(\frac{-e^2}{\varepsilon r k T}\right)\left(1 + \frac{e^3 E}{\varepsilon (kT)^2} + \cdots\right),$$

where r is the initial thermalization length. Taking $\varepsilon = 5.9$ for the b crystalline direction [14], the Onsager theory fits the data for an initial thermalization length of $r = 40$ Å. Considering that r is the only adjustable parameter, this is an extremely good fit. Using the Poole-Frenkel model, where a balance of emission and recombination rates give

$$Y^{-1} = 1 + A \exp\left\{-\left(\frac{e^3 E}{\varepsilon (kT)^2}\right)^{1/2}\right\},$$

a field dependence simply too strong to fit the data.

The Onsager model divides the generation step into three parts: (a) creation of

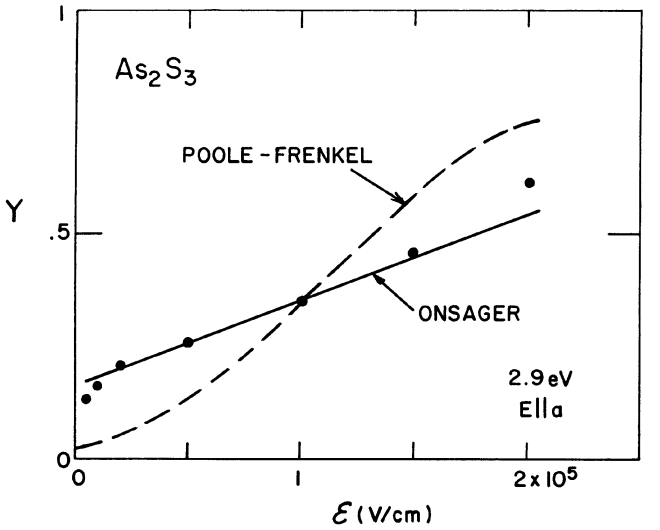

Fig. 19. Field dependence of the photoyield in As_2S_3 for strongly absorbed photons. The solid and dashed lines are, respectively, Onsager and Poole-Frenkel fits to the data.

a hot electron-hole pair through optical excitation, (b) scattering by lattice vibrations or defects causing thermalization of the pair at some initial separation, and (c) motion of carriers by diffusion and drift in the pair's mutually attractive potential plus applied potential. The ultimate fate of any carrier pair is either recombination or dissociation. As shown by Onsager [42] for a three-dimensional Coulomb potential, the recombination rate is field independent whereas the dissociation rate has a finite zero-field value and increases with the applied field. In other work, it is discussed how the thermalization length is related to the microscopic mobility [41].

Transient photoconductivity experiments on crystalline As_2S_3 [43] have been performed to establish the carrier mobilities. Results of these time-of-flight transport measurements are shown in Figure 20 for electron motion normal to the layers. The experiment is done with the sample sandwiched between two transparent contacts. A sheet of charge is created at one contact by flash illumination with strongly absorbed light, and is forced to drift through the solid by an applied field. This is the standard drift mobility measurement [44] in which the mobility of the transiting carrier is defined as the ratio of the carrier velocity to the applied field. In Figure 20 the inverse transit time is plotted against the applied voltage, and the fact that the data define a straight line passing through the origin means that the mobility is well-defined and field independent. The value of the electron mobility shown is 1.0 cm^2/volt-sec., and was very reproducible from sample to sample. Much more spread was observed for hole mobilities, with measured values varying from 0.3 to 3.0 cm^2/volt-sec. [43].

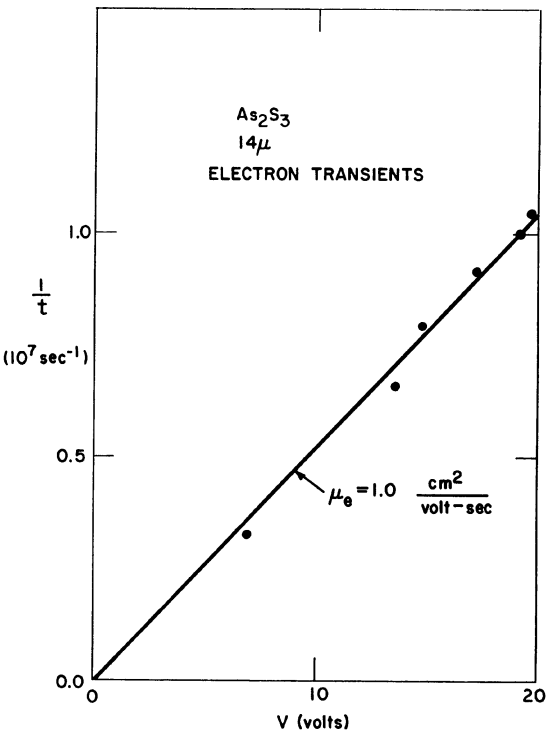

Fig. 20. Reciprocal transit time versus applied voltage observed in time-of-flight measurements of electron transport perpendicular to the layers in As_2S_3.

These mobilities are typical of those observed for molecular solids such as anthracene [44], and reflect the fact that the carrier transport in this case is controlled by the weak interlayer interactions. For these solids the mobilities are too low for the carrier motion to be considered to be completely band-like, and too high to be completely hopping. The usual treatment is to consider the carrier motion to be in polaron bands [45] in which the carrier moves so slowly that a lattice polarization cloud moves with it. Calculations have thus far been limited to organic crystals [46], but should also apply to inorganic layer crystals for carrier transport normal to the layers.

5.3. Internal photoemission

An experiment related to photoconductivity is internal photoemission, photoinjection from metals into solids. We have already seen in Section 5.1 that carriers can be photoinjected from liquid contacts into the solid. With metal contacts the situation theoretically could be much simpler, but in practice it is generally much more complicated because of the added variable of the unknown interface

chemistry. In recent years, a phenomenology [47] of metal-insulator interfaces has been proposed which attempts to relate interface states to the ionicity of the compound. Since Pauling ionicity [48] is itself derived from chemical heats of formation, this phenomenology may have more to do with the chemical stability or instability of the interface than with the ionicity of the semiconductor. The internal photoemission data [49] that follows will be examined with the chemical stability of the interface in mind, but first let us review some of the fundamentals of the internal photoemission phenomenon.

Internal photoemission has been used largely for determination of barrier heights for carrier injection in metal-insulator systems [50]. The technique is very similar to photoemission from metals into vacuum, except that the hot carriers (electrons *or* holes) are injected from the metal directly into the transport bands of the insulator. In the absence of Fermi-level stabilization at the surface [47], the photoemission threshold is a direct measure of the energy separation of the Fermi level in the metal and the bottom of the conduction band (for electron injection) or the top of the valence band (for hole injection). Since the hot carriers are injected into a solid instead of vacuum, they can lose energy through scattering events. Through back scattering, diffusion, or the attractive force of the image potential, some of the injected carriers will be returned to the metal and will not be collected. The collection efficiency will be field dependent and should saturate at a field determined by the microscopic mobility of the injected carrier in the solid. A thorough discussion of the field dependence of the injection process is beyond the scope of this review; the reader is referred to a recent treatment given by Blossey [41].

For internal photoemission, the primary step is the creation of hot carriers in the metal. These hot carriers will have an equal probability of travelling in all directions, and only a certain fraction of the carriers will have enough kinetic energy normal to the interface to overcome the potential difference and enter the semiconductor. The standard assumption for internal photoemission calculations is that the transition matrix element in the metal varies little with photon energy over the region of interest. This approximation is certainly valid over a narrow spectral region, and if we focus our attention to photon energies just above threshold it is easy to show that the photoyield Y (carriers injected per incident photon) is proportional to $(h\nu - E_0)^2$. Plots of $Y^{1/2}$ versus $h\nu$ are used for determining E_0, the barrier height for carrier injection.

The general features of the photoinjection yield spectra are shown in Figure 21 for electron injection from gold into As_2S_3. The injection current is observed in the transparent region of the crystal, $h\nu < 2.6\,\text{eV}$. The experimental arrangement is a sandwich cell configuration with a transparent liquid contact on the illuminated side of the sample and an evaporated metal contact on the back. In this arrangement, the light (for $h\nu < 2.6$ eV) passes through the crystal and is absorbed in the back metal contact creating hot carriers. Depending on the bias, either holes or electrons are then injected from the contact into the sample. As seen in

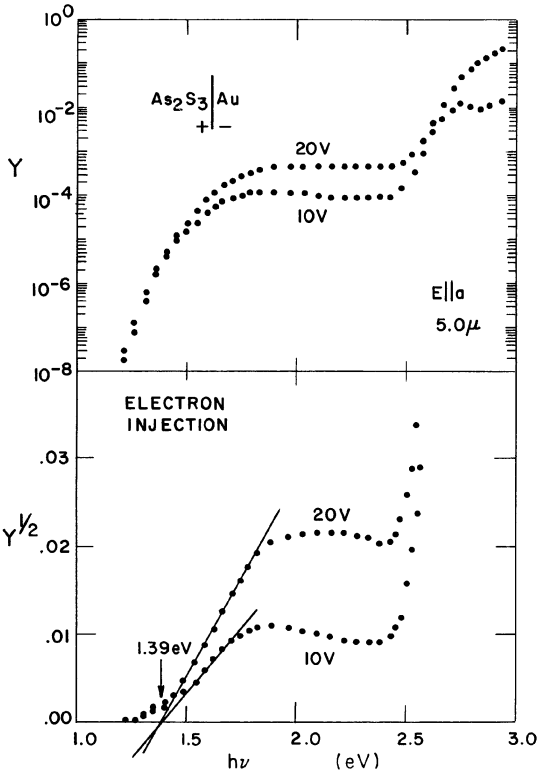

Fig. 21. Photoyield spectra for electron injection from Au into As_2S_3.

Figure 21, the amplitude of the injection current depends on field, but the extrapolated threshold of 1.39 eV for electron injection from Au into As_2S_3 does not. Results obtained with the bias reversed yield a hole injection threshold of 1.24 eV. Since the sum of the two thresholds is approximately the room-temperature E_G of As_2S_3 (as discussed at the end of Section 4.1), any band-bending near the As_2S_3—Au interface is negligible and there is certainly no evidence of a chemical interface region which inhibits carrier injection. The band structure of the Au—As_2S_3 interface is perceived to be as shown in Figure 22. The work function of 6.06 eV for As_2S_3, as calculated from the sum of the Au work function and the hole injection barrier, is similar to that measured for amorphous As_2Se_3 by vacuum photoemission [51].

In addition to Au, many other metals with various work functions and electronegativities can be used as contacts, and their metal-insulator interface barriers investigated. It has been empirically observed that semiconductors possess interface barriers which approximately obey the relationship

$$\phi_B = SX_M + \text{const.},$$

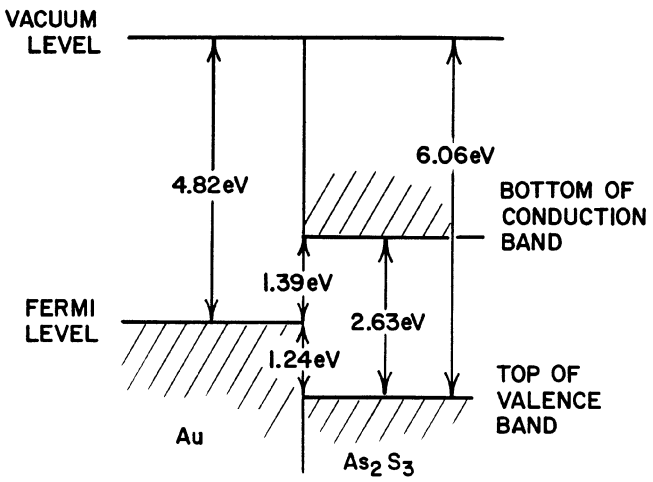

Fig. 22. Schematic energy-level diagram at the interface between an orpiment crystal and a gold contact.

where ϕ_B is the interface barrier, X_M is the metal electronegativity, and S is a constant slope which varies between 0 and 1 depending on the solid [47]. Solids with $S \approx 0$ have high densities of interface states allowing complete Fermi level stabilization at the interface ('pinning' of the Fermi level), while solids with $S \approx 1$ have very low densities of interface states. Arguments [47] relating electron delocalization, surface states in vacuum, and interface states are less than convincing since it is very unlikely that there is any relationship between states on a clean surface in vacuum and the interface states formed between a metal and a semiconductor or insulator [52]. It seems much more probable that the propensity of a solid to form interface states is determined by the *chemistry* of the interface. Although the value of S has been shown to correlate directly with the ionicity of

TABLE II

Reactivity[a] of selected metals with crystalline As_2S_3

Metal electronegativity	Reaction	Heat of reaction ΔE
1.5	$2Al + As_2S_3 \rightarrow 2As + Al_2S_3$	−5.8 eV
1.7	$2In + As_2S_3 \rightarrow 2As + In_2S_3$	−2.7 eV
1.9	$6Cu + As_2S_3 \rightarrow 2As + 3Cu_2S$	−0.7 eV
1.9	$6Ag + As_2S_3 \rightarrow 2As + 3Ag_2S$	+0.7 eV
2.2	$Pd + As_2S_3 \rightarrow$	
2.4	$Au + As_2S_3 \rightarrow$	

[a] Heats of formation used for determining the heats of reaction were obtained from NBS Technical Notes 270-3 (1968) and 270-4 (1969): *Selected Values of Chemical Thermodynamic Properties.*

the solid [47], that value can just as easily be shown to correlate with compound stability.

For As_2S_3, six metals have been evaporated as contacts [49]. In order of increasing electronegativity, these are Al, In, Cu, Ag, Pd, and Au. Table II shows that the first three metals (Al, In, Cu) have exothermic reactions with As_2S_3, while the other three (Ag, Pd, Au) should be less reactive. Interestingly enough, the Al interface traps holes, the Cu interface turns black, and the In contact exhibits injection currents near threshold which don't scale with those observed with Ag, Pd, and Au contacts. All of these effects are probably due to the chemical formation of a new phase in the interface region.

The photoinjection yields for both electrons and holes are shown for Pd in Figure 23. The insert shows the band bending which would account for the observed thresholds. Figure 24 compares the hole injection thresholds of Pd and the other two inert (relative to As_2S_3) metals. The insert shows that these thresholds vary linearly with metal electronegativity, with unity slope. From this we conclude that *inert* surfaces yield unity slope but that *reactive* surfaces will yield a slope less than unity. Finally, in Figure 25, we show that for these three metals As_2S_3 does not fit on the Kurtin, McGill, Mead [47] 'universal' curve. Including reactive metals lowers the S value for As_2S_3, but does not bring it down

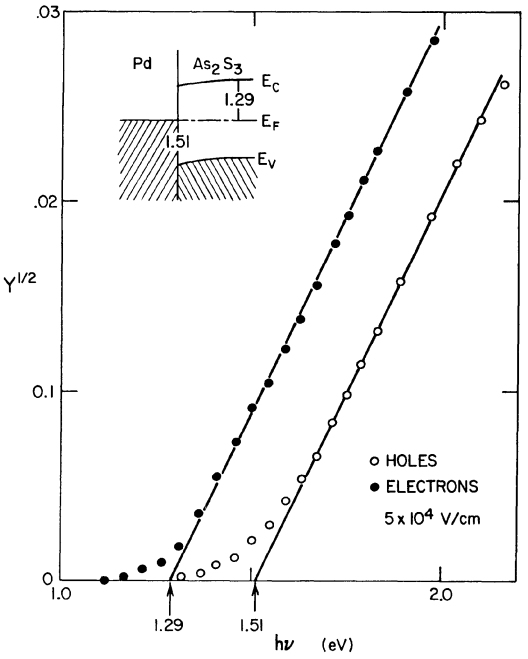

Fig. 23. Near-threshold photoyield spectra for injection of electrons and holes from Pd into As_2S_3. The insert indicates how band bending near the interface can increase the sum of the two thresholds to a value exceeding the crystal's bandgap.

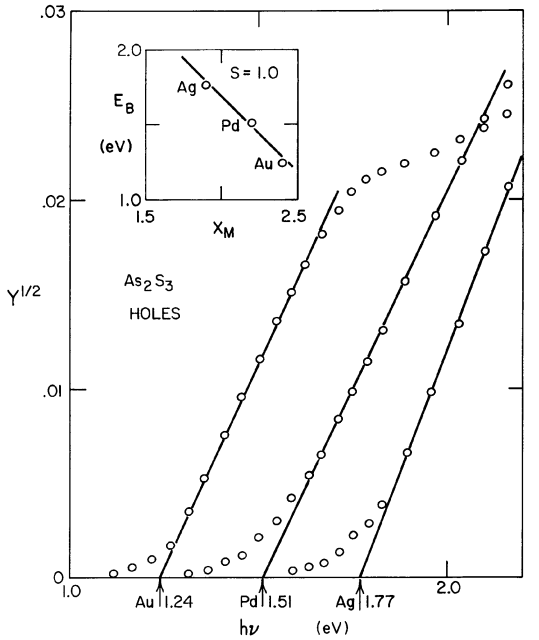

Fig. 24. Photoyield spectra near the threshold for injection of holes into As_2S_3 from electrodes of gold, palladium, and silver. The insert shows the correlation of the threshold energy with the Pauling electronegativity of the metal.

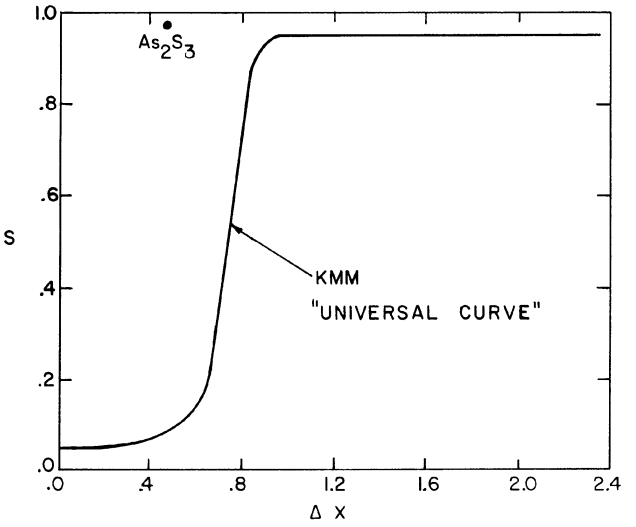

Fig. 25. Deviation of the layer semiconductor As_2S_3 from the covalent-ionic transition curve of Kurtin, McGill, and Mead [47] for the correlation of electrical interface behavior with semiconductor ionicity. ΔX is the electronegativity difference between the elemental components of a compound semiconductor, S is the slope of the interface-barrier versus metal-electronegativity characteristic (such as that contained in the insert in Figure 24) observed with various contacts to the semiconductor.

close to the KMM curve. The question arises: Does the value of S for a solid represent some average of reactive and inert contacts, and if so, how do you decide how many metals to include to get the correct value? Our experience with As_2S_3 suggests that S is not necessarily a meaningful parameter, and that the ϕ_B-versus-X_M behavior depends upon whether inert or reactive metals are involved.

6. Summary

In concluding our review of the optical properties and photoconductivity of arsenic chalcogenide layer crystals, we will not attempt a reprise of all the main themes treated herein. Instead we will comment on overall aspects of the current level of understanding of these solids, and will also point out a few specific possible new lines of fruitful activity (using restraint in this, since nothing is easier than to suggest many man-years of work in a few short sentences) in the hope of encouraging research in such directions.

Because of their unique structure and low symmetry, As_2S_3 and As_2Se_3 were the first layer crystals for which the significance of the diperiodic symmetry was appreciated and fully explored. Because of their intimate relationship to (and value as illuminating models of) technologically-important glasses, their optical and photoelectronic properties have come under increasing experimental investigation in recent years. Several basic elements of their electronic structure, such as the dominance of direct transitions at the interband threshold and the valence-band division between bonding and nonbonding states, have come to light as a result. A marked contrast is apparent, however, in comparing the wealth of spectral information contained in Figures 4–12 with the plain appearance of the simple models of Figures 13 and 14. This reveals a need for useful theoretical work to provide, for example, band-structure guidelines for interpretation of the interband spectra. Besides the question of the two-dimensional band structure of the covalently-bonded extended layer, a theoretical attack on the data bearing on layer–layer electronic overlap is clearly needed to improve our meager understanding of the weak interlayer bonding which holds these crystals together.

Although our knowledge of the optical properties for the two in-plane polarizations is now quite extensive, information about the elusive out-of-plane polarization remains sketchy. This is an experimental problem created by the great difficulty of obtaining good surfaces perpendicular to the layers, and may require a drastic solution such as the lengthy oblique-incidence technique devised by Greenaway *et al.* [53] for the out-of-plane polarization in graphite. Their results for graphite were dramatic since that classic layer crystal, which has, of course, the optical properties of a semimetal for light polarized parallel to the layers, was found to have the optical properties of an insulator for the perpendicular polarization. For the layer chalcogenides the results will not be so spectacular, since insulating optical properties are involved for all polarizations. However the difference between out-of-plane and in-plane optical properties will be in the

same direction (more insulating for $E \| b$, as indicated by, for example, the dielectric constant data of Table I), and the out-of-plane spectrum will shed new light on the connection between crystalline and amorphous forms.

A situation somewhat the reverse of the optical one, but caused by the same underlying reason (the severe anisotropy of a layer crystal) exists with respect to the transport properties. Carrier mobilities perpendicular to the layers are known, but not parallel to the layers. The former are found to be characteristic of intermolecular transport (≈ 1 cm^2/volt-sec), while the latter should be characteristic of the much easier broad-band transport of covalent semiconductors. This orders-of-magnitude mobility anisotropy should be confirmed, and it is also likely that interesting two-dimensional effects will be observed in the intralayer transport.

There is an even more fascinating question which concerns the electrical interface behavior observed with metal contacts to a layer semiconductor. We have discussed the importance of chemical stability at the interface, and have demonstrated that the inert-metal interface behavior of As_2S_3 does *not* conform to a current picture of a covalent-ionic transition in the observed behavior. As seen in Figure 25, although As_2S_3 lies well to the covalent side of the transition, its electrical interface behavior is similar to that seen for ionic semiconductors. Now these results are for interfaces parallel to the layer planes, and it could be argued that the covalent bonding doesn't enter since such an interface involves no broken intralayer bonds. If this idea were correct, it would suggest that molecular-solid semiconductors would show 'ionic-type' interface behavior no matter how covalent the intramolecular bonding. A definitive test would be provided by measurements on metal-As_2S_3 interfaces perpendicular to the layers. Such layer-cutting interfaces, which involve broken bonds in a way similar to that for 3_D-network germanium-type semiconductors, could reveal the opposite behavior (i.e. Fermi-level pinning) to that observed for layer-parallel interfaces. If this is so, it would salvage the idea of the covalent-ionic interface-behavior transition, with the important proviso established that molecular interfaces behave 'ionically'. It would also provide yet another fine example of the enormously antithetical behavior of intralayer and interlayer electronic effects in a layer crystal.

References

1. R. Zallen, M. L. Slade, and A. T. Ward: *Phys. Rev.* **B3** (1971), 4257.
2. R. Zallen: in Proceedings of the Twelfth International Conference on the Physics of Semiconductors (Stuttgart), Teubner, Stuttgart, 1974, p. 621.
3. W. H. Zachariasen: *J. Am. Chem. Soc.* **54** (1932), 3841.
4. N. Morimoto: *Mineral J. (Sapporo)* **1** (1954), 160.
5. A. A. Vaipolin: *Sov. Phys. – Crystallography* **10** (1966), 509.
6. J. I. Hanoka, K. Vedam, and H. K. Henisch: *J. Phys. Chem. Solids, Supplement* (1967), 369.
7. R. Zallen and M. Slade: *Phys. Rev.* **B9** (1974), 1627.

8. S. Nakashima, H. Mishima, and A. Mitsuishi: *J. Raman Spectrosc.*, **1** (1973), 325.
9. E. A. Wood: *Bell System Tech. J.* **43** (1964), 541.
10. B. L. Evans and P. A. Young: *Proc. Roy. Soc.* **A297** (1967), 230.
11. R. Zallen, R. E. Drews, R. L. Emerald, and M. L. Slade: *Phys. Rev. Letters* **26** (1971), 1564.
12. J. Perrin, J. Cazaux, and P. Soukiassian: *Phys. Status Solidi* **B62** (1974), 343.
13. I. Chen and R. Zallen: *Phys. Rev.* **173** (1968), 833; E. Burstein, M. H. Brodsky, and G. Lucovsky: *Intern. J. Quantum Chem.* **15** (1967), 759; W. Cochran: *Nature* **191** (1961), 60.
14. M. Abkowitz, D. F. Blossey, and A. I. Lakatos: *Phys. Rev.* **B12** (1975), 3400.
15. P. C. Taylor, S. G. Bishop, D. L. Mitchell, and D. Treacy: in Proceedings of the Fifth International Conference on Amorphous and Liquid Semiconductors (Garmisch), Taylor and Francis, London, 1974, p. 1267; D. Treacy and P. C. Taylor: *Phys. Rev.* **B11** (1975), 2941.
16. R. E. Drews, R. L. Emerald, M. L. Slade, and R. Zallen: *Solid State Commun.* **10** (1972), 293.
17. G. B. Fisher: to be published.
18. S. G. Bishop and N. J. Shevchik: in Proceedings of the Twelfth International Conference on the Physics of Semiconductors (Stuttgart), Teubner, Stuttgart, 1974, p. 1017.
19. R. Zallen, M. L. Slade, R. L. Emerald, and R. E. Drews: unpublished data.
20. I. S. Gorban' and R. A. Dashkovskaya: *Sov. Phys. – Solid State* **6** (1965), 1895.
21. R. F. Shaw, W. Y. Liang, and A. D. Yoffe: *J. Non-Cryst. Solids* **4** (1970), 29.
22. A. J. Grant and A. D. Yoffe: *Solid State Commun.* **8** (1970), 1919.
23. B. T. Kolomiets and E. M. Raspopova: *Sov. Phys. – Semicond.* **4** (1970), 124.
24. W. Paul: in Proceedings of the Enrico Fermi Summer School on Optical Properties of Solids, Academic Press. New York, 1966, p. 257; R. Zallen and W. Paul: *Phys. Rev.* **155** (1967), 703.
25. J. M. Besson, K. P. Jain, and A. Kuhn: *Phys. Rev. Letters* **32** (1974), 936.
26. R. Zallen: *Phys. Rev.* **B9** (1974), 4485.
27. M. P. Lisitsa, A. M. Yaremko, G. G. Tarasov, M. Ya. Valakh, and L. I. Berezhinskii: *Sov. Phys – Solid State* **14** (1973), 2744.
28. E. Mooser and W. B. Pearson: in Progress in Semiconductors, Vol. 5, Wiley, New York, 1960, p. 104; M. Kastner: *Phys. Rev.* **B7** (1973), 5237.
29. A. A. Vaipolin and E. A. Porai-Koshits: *Sov. Phys.–Solid State* **2** (1961), 1500; *and* **5** (1963), 178; and **5** (1963), 497; J. I. Petz, R. F. Kruh, and G. C. Amstutz: *J. Chem. Phys.* **34** (1961), 526; T. E. Hopkins, R. A. Pasternak, E. S. Gould, and J. R. Herndon: *J. Phys. Chem* **66** (1962), 733.
30. C. E. Moore: Atomic Energy Levels, NBS Circular No. 467, U.S. Govt. Printing Office, Wash., D.C., 1952, 1958; W. Lotz: *J. Opt. Soc. Am.* **60** (1970), 206.
31. J. Dresner and G. B. Stringfellow: *J. Phys. Chem. Solids* **29** (1968), 303; J. Feinleib, J. Deneufville, S. C. Moss, and S. R. Ovshinsky: *Appl. Phys. Lett.*, **18** (1971), 254; J. S. Berkes, S. W. Ing, and W. J. Hillegas: *J. Appl. Phys.* **42** (1971), 4908.
32. I. Chen: *Phys. Rev.* **B8** (1973), 1440.
33. P. Nielsen: *Bull. Am. Phys. Soc.* **17** (1972), 113.
34. D. F. Blossey and R. Zallen: *Phys. Rev.* **B9** (1974), 4306.
35. D. F. Blossey: *Chem. Phys. Lett.* **25** (1974), 593.
36. R. C. Enck: *Phys. Rev. Lett.* **31** (1973), 220; D. M. Pai and S. W. Ing, Jr.: *Phys. Rev.* **173** (1968), 729; M. D. Tabak and P. J. Warter: *Phys. Rev.* **173** (1968), 899.
37. S. W. Ing, Jr., J. H. Neyhart, and F. W. Schmidlin: *J. Appl. Phys.* **42** (1971), 696.
38. P. J. Melz: *J. Chem. Phys.* **57** (1972), 1694.
39. R. H. Batt, C. L. Braun, and J. F. Hornig: *J. Chem. Phys.* **49** (1968), 1967; and *Appl. Opt. Suppl.* **3** (1969), 20; R. R. Chance and C. L. Braun: *J. Chem. Phys.* **59** (1973), 2269.
40. H. Kallman and M. Pope: *J. Chem. Phys.* **32** (1960), 300; W. Mehl, J. M. Hale, and J. S. Drury: *Ber. Bunsenges. Physik. Chem.* **73** (1969), 855.
41. D. F. Blossey: *Phys. Rev.* **B9** (1974), 5183.
42. L. Onsager: *Phys. Rev.* **54** (1938), 554; and *J. Chem. Phys.* **2** (1934), 599.
43. D. F. Blossey and R. C. Enck: unpublished data.
44. R. G. Kepler: *Phys. Rev.* **119** (1960), 1226.
45. T. Holstein: *Ann. Phys. (N.Y.)***8** (1959), 343.
46. R. W. Munn and W. Siebrand: *J. Chem. Phys.* **52** (1970), 6391.
47. S. Kurtin, T. C. McGill, and C. A. Mead: *Phys. Rev. Lett.* **22** (1969), 1433.

48. L. Pauling: *The Nature of the Chemical Bond*, Cornell Univ. Press, New York, 1967.
49. D. F. Blossey: to be published.
50. R. W. Williams: in *Semiconductors and Semimetals*, Vol. 8, Academic Press, New York, 1970.
51. P. Nielsen: *Solid State Commun.* **9** (1971), 1745.
52. J. C. Phillips: *Solid State Commun.* **12** (1973), 861; *Surface Sci.* **37** (1973), 24; *J. Phys. Chem. Solids* **34** (1973), 1051.
53. D. L. Greenaway, G. Harbeke, F. Bassani, and E. Tosatti: *Phys. Rev.* **178** (1969), 1340.